Combining spectroscopic and photometric surveys using angular cross-correlations – II. Parameter constraints from different physical effects

Martin Eriksen[1,2]★ and Enrique Gaztañaga[1]★

[1]*Institut de Ciències de l'Espai (IEEC-CSIC), E-08193 Bellaterra (Barcelona), Spain*
[2]*Leiden Observatory, Leiden University, PO Box 9513, NL-2300 RA Leiden, the Netherlands*

ABSTRACT

Future spectroscopic and photometric surveys will measure accurate positions and shapes of an increasing number of galaxies. In the previous paper of this series, we studied the effects of redshift space distortions (RSD), baryon acoustic oscillations (BAO) and weak gravitational lensing (WL) using angular cross-correlation. Here, we provide a new forecast that explores the contribution of including different observables, physical effects (galaxy bias, WL, RSD, BAO) and approximations (non-linearities, Limber approximation, covariance between probes). The radial information is included by using the cross-correlation of separate narrow redshift bins. For the auto-correlation the separation of galaxy pairs is mostly transverse, while the cross-correlation also includes a radial component. We study how this information adds to our figure of merit (FoM), which includes the dark energy equation of state $w(z)$ and the growth history, parametrized by γ. We show that the Limber approximation and galaxy bias are the most critical ingredients to the modelling of correlations. Adding WL increases our FoM by 4.8, RSD by 2.1 and BAO by 1.3. We also explore how overlapping surveys perform under the different assumptions and for different FoMs. Our qualitative conclusions depend on the survey choices and scales included, but we find some clear tendencies that highlight the importance of combining different probes and can be used to guide and optimize survey strategies.

Key words: dark energy – dark matter – large-scale structure of Universe.

1 INTRODUCTION

The expansion of the Universe provides a challenge for cosmology and fundamental physics. Understanding the recent accelerated expansion of the Universe is connected to dark matter and dark energy (DE), either by determining their properties or by providing an alternative theory. There is no scarcity of models, but no model beyond Λ cold dark matter (CDM) has emerged as a natural candidate to explain the cosmic acceleration.

Galaxy surveys are designed to probe cosmology in different manners. Weak gravitational lensing (WL) of foreground matter affects the galaxy shapes. Observing the WL through galaxy shapes (shear) (Massey et al. 2007; Schrabback et al. 2010) requires deep imaging surveys like Dark Energy Survey (DES) and the upcoming *Euclid* and Large Synoptic Survey Telescope (LSST). Further, overdensities of dark matter attract nearby galaxies, which creates an additional peculiar velocity. The radial component of the extra velocity results in a shift in redshift, which is the effect of redshift space distortions (RSD). Optimal measurement of RSD requires

accurate redshift and the method is most suitable for spectroscopic surveys.

The lensing efficiency has a broad kernel and the shear–shear lensing signal can be analysed in 5–10 broad redshift bins. The RSD signal is traditionally analysed using power spectrum analysis in 3D comoving space, which includes a cosmology-dependent conversion transformation of angles and redshift to the 3D comoving distances. As shown in Eriksen & Gaztañaga (2015, Paper I, and references therein), angular correlations can also be used to measure RSD. A previous study by Asorey et al. (2012) found that angular correlations in narrow redshift bins can recover most of the information in the 3D power spectrum. In these papers, we use the angular correlation for both the photometric (WL) and spectroscopic (RSD, WL) survey.

Using a single set of observables for WL and RSD has several advantages. For overlapping surveys, the galaxies trace the same matter fluctuations, which introduce a covariance between the surveys. Particular care is needed to not double counting information when jointly observing shear–shear in the lensing survey, the 3D power spectrum for the spectroscopic survey and 2D correlations for the counts–shear cross-correlations between the two. For example, counting the modes is insufficient if including photo-z

★E-mail: marberi@strw.leidenuniv.nl (ME); gazta@ieec.uab.es (EG)

effects in the 3D sample since the photo-z affects the radial and transverse modes differently.

Several groups have explored combining WL and spectroscopic surveys (Bernstein & Cai 2011; Cai & Bernstein 2012; Gaztañaga et al. 2012; de Putter, Doré & Takada 2013; Font-Ribera et al. 2013; Kirk et al. 2013). In overlapping surveys (same-sky), one can cross-correlate the observables, e.g. galaxy counts from the two surveys or galaxy counts from the spectroscopic sample with background shear from the lensing survey. Overlapping samples further reduce the sample variance (McDonald & Seljak 2009). While non-overlapping surveys benefit from larger area, several authors find stronger parameter constraints when combining WL and spectroscopic surveys over the same area. In this paper, we study the importance of different physical effects for overlapping and non-overlapping surveys, while the paper Eriksen & Gaztañaga (2014) elaborates on the benefit of overlapping surveys.

Galaxies are theoretically (Scoccimarro et al. 2001) and observationally expected to form in overdense regions. Unlike shear which is affected by all foreground matter, the galaxy counts relate to the underlying matter distribution at a given redshift. The negative side of probing cosmology with the galaxy counts is requiring to understand and marginalize over uncertainties in the relation between matter and galaxy overdensities, the galaxy bias (Gaztañaga et al. 2012). One can either approach the galaxy bias by using only the BAO peak (Seo & Eisenstein 2003, 2007) or parametrize the bias (Shoji, Jeong & Komatsu 2009). In this paper, we use the full galaxy correlation and measure the bias parameters by combining Large-scale structure (LSS) and lensing in a multiple tracer analysis.

Magnification changes the overdensities of number counts through two WL effects. In a magnitude-limited sample, lensed galaxies appear brighter and enter into the sample when magnified over the magnitude cut. The magnification also magnifies the area which reduces the number density. In the Sloan Digital Sky Survey (SDSS) sample, magnification has been observed by correlating foreground galaxies with background quasars (Scranton et al. 2005; Ménard et al. 2010). While the shear–shear signal has less noise, magnification provides an additional signal which is already present in the galaxy catalogues. This paper, in a similar way to Gaztañaga et al. (2012) and Duncan et al. (2014), will study the benefits of magnification when combining the analysis of spectroscopic and photometric surveys in angular correlations.

Photometric surveys conventionally use broad-band filters. Two upcoming surveys, PAU[1] and J-PAS,[2] plan to measure photometry for galaxies in 40–50 narrow (100–130 Å) bands. For PAU the resulting photo-z precision is $\sigma_{68} \approx 0.0035(1 + z)$ for $i_{AB} \leq 22.5$ (Martí et al. 2014). In addition, the PAUcam broad-bands ($ugrizY$) has an anticipated photo-z accuracy of $\sigma_{68} = 0.05(1 + z)$ for $22.5 < i_{AB} < 24.1$. The PAU survey at the William Herschel Telescope can cover about 200 sq. deg. to $i_{AB} < 22.5$ in narrow bands and $i_{AB} < 24$ with broad-bands in 100 nights. This defines two magnitude-limited populations of bright (B) galaxies ($i_{AB} < 22.5$) and faint (F) galaxies ($22.5 < i_{AB} < 24$) similar to two overlapping spectroscopic and photometric surveys.

This paper (Paper II) is part of a three-paper series. Paper I dealt with modelling of the correlation function, focusing in particular on the effect of RSD, BAO and the Limber approximation in narrow bins. Here (Paper II) we forecast the relative impact of WL, RSD and BAO in upcoming cosmological surveys. A third paper (Eriksen

& Gaztanaga, in preparation, Paper III) studies the impact of galaxy bias, while a separate paper (Eriksen & Gaztañaga 2014) focuses on the benefit of overlapping surveys.

This paper is organized in the following manner. Section 2 presents the assumptions, which include Fisher matrix formalism, forecast assumptions and nomenclature. In Section 3, we compare the relative contribution of the different effects (including WL, RSD, BAO, magnification) and the Limber approximation. Section 4 gives the conclusion.

2 FORECAST ASSUMPTIONS

This section first presents the assumptions of fiducial cosmology, galaxy bias parametrization, galaxy samples, survey definitions, cuts in non-linear scales and the Fisher forecast. Paper I included the theoretical expressions for the C_l cross-correlations and they are therefore not repeated here. In this section, we also define the figures of merit (FoMs) and the nomenclature (e.g. F×B, F+B) used throughout the paper.

2.1 Fiducial cosmological model

The cosmological model assumed is wCDM,[3] which is General Relativity (GR) with CDM and a DE model with an equation of state (EoS) $w \equiv \frac{\rho_{DE}}{\rho_{DE}}$. The main observables are C_l cross-correlations of fluctuations $\delta(z, k)$, which depend on the initial power spectrum, distances and the growth of fluctuations. For a Friedmann–Lemaître–Robertson–Walker metric (Dodelson 2003), the Hubble distance is

$$H^2(z) = H_0^2[\Omega_m a^{-3} + \Omega_k a^{-2} + \rho_{DE}(z)] \quad (1)$$

$$\rho_{DE} = \Omega_{DE} a^{-3(1+w_0+w_a)} \exp(-3w_a z/(1+z)), \quad (2)$$

where the last equation expresses the dark energy density using the parametrization

$$w(z) = w_0 + w_a(1 - a) \quad (3)$$

from Chevallier & Polarski (2001) and Linder (2003, 2005) for the DE EoS. Overdensities of matter grow because of gravitational attraction and at large (linear) scales the equation determining the growth has the solutions (Heath 1977; Peebles 1980)

$$\delta(z) = D(z)\delta(0), \quad (4)$$

where $D(z)$ is defined through

$$f \equiv \frac{d \ln(D)}{d \ln(a)} = \frac{\dot{\delta}}{\delta} \equiv \Omega_m^\gamma(a). \quad (5)$$

Normalizing the growth to $D(z = 0) = 1$, we have

$$D(z) = \exp\left[-\int_a^1 d \ln a f(a)\right]. \quad (6)$$

In these papers [and previously in Gaztañaga et al. (2012)], the growth is parametrized through the parameter γ in equation (5), which is $\gamma \approx 3/11 \approx 0.55$ in GR with a cosmological constant. For

---

[3] For the fiducial cosmology, we use the values $\Omega_m = 0.25$, $\Omega_b = 0.044$, $\Omega_{DE} = 0.75$, $h = 0.7$, $w_0 = -1$, $w_a = 0$, $n_s = 0.95$ and $\sigma_8 = 0.8$, which correspond to the cosmological model in the MICE (http://www.ice.cat/mice) simulation.

example, the DGP model (Dvali, Gabadadze & Porrati 2000) proposes to explain the cosmological acceleration through embedding the ordinary 3+1 dimensional Minkowski space in a 4+1 dimensional Minkowski space. Alternatively modified gravity, which we have left of future work, can be parametrized by the Bardeen potentials (Bardeen 1980). Adjusting free parameters in modified gravity can potentially fit the right expansion history (equation 2), but it is more difficult to simultaneously fit the expansion and growth history (equation 6). Constraining both the growth and expansion history is therefore important to discriminate between different modified gravity models.

2.2 Non-linear scales

On lager scales fluctuations are linear. In contrast, for high-density regions the structures collapse in a non-linear manner. As a result, predicting the non-linear power spectrum requires either simulations (Springel 2005), perturbation theory (Crocce 2007) or fitting functions to simulations (Heitmann et al. 2010, 2009; Lawrence et al. 2010). Here the forecast uses the Eisenstein–Hu (Eisenstein & Hu 1998) linear power spectrum. In Appendix A, we test the effect of including the non-linear contribution.

Even when including non-linear power spectrum contributions, one needs to limit the maximum k_{max} (or minimum r_{min}) scale. The Halofit II model is calibrated to 5 per cent accuracy for $k \leq 1\,h\,\mathrm{Mpc}^{-1}$ at $0 \leq z \leq 10$. Further, we also want to limit observations to scales where the bias (see Section 2.3) is scale independent. Here and in other papers of this series, the maximum scale is defined through

$$\sigma(R_{min}, z) = 1, \tag{7}$$

where $\sigma(R, z)$ is the fluctuation amplitude smoothed with a Gaussian kernel on a scale R. From $k = l/\chi(z)$, we have

$$k_{max}(z) = \frac{R(0)_{min}}{R(z)_{min}} k_{max}(0), \tag{8}$$

where $k_{max}(0) = 0.1\,h^{-1}\mathrm{Mpc}$ is an overall normalization. In the MICE cosmology and Eisenstein–Hu power spectrum, then

$$k_{max}(z) = \exp(-2.29 + 0.88z) \tag{9}$$

is a good fit for the k_{max} limit. The conversion to an l_{max} for which correlations to include is done with

$$k_{max} = \frac{l_{max} + 0.5}{r(z_i)} \tag{10}$$

which uses the scale contributing to LSS and counts–shear correlations in the Limber equation (see Paper I). For cross-correlations, we use the minimum k_{max} from the two redshift bins. The forecast is restricted to $10 \leq l \leq 300$ and in addition applies to the cut above, including for the shear–shear correlations. To save time, the forecast uses $\Delta l = 10$. We have tested that the discrete l-values have minimal impact on the forecast.

2.3 Galaxy bias

Galaxy overdensities δ are in a local bias model (Fry & Gaztanaga 1993) related to matter overdensities δ_m through

$$\delta(k, z) = b(z, k)\delta_m(k, z), \tag{11}$$

where the bias $b(k, z)$ can in general depend on scale and redshift. Each subset of galaxies, of galaxy population, can have different bias since galaxy types (e.g. elliptical and spirals) cluster and evolve

differently. When defining populations by magnitude cuts, as we do, the bias also differs because each population contains another mixture of galaxies.

The two galaxy populations (see Section 2.6) use a different bias and bias nuisance parameters. We use one bias parameter per redshift bin and galaxy population, no scale dependence and no additional bias priors. In addition, the bias can include a stochastic component. A commonly used measure of non-linearity and the stochasticity is

$$r \equiv \sqrt{\frac{C_{\delta m}}{C_{\delta\delta}C_{\delta m}}}, \tag{12}$$

where $C_{\delta\delta} \equiv \langle\delta\delta\rangle$, $C_{\delta\delta_m} \equiv \langle\delta m\rangle$ and $C_{mm} \equiv \langle\delta_m\delta_m\rangle$, respectively, are the counts–counts, counts–matter and matter–matter correlations. For a deterministic and linear bias, then $r = 1$. In Gaztañaga et al. (2012), we showed by theoretical models and also simulations that the stochasticity can be treated as a re-normalization of the bias. Thus, we fix the stochasticity to $r = 1$ and explore the impact of r in Paper III.

2.4 Fisher matrix forecast

The Fisher matrix is a simple and fast method to estimate parameter uncertainties. Deriving the Fisher matrix follows from a Gaussian approximation of the likelihood expanded around the fiducial value. Sampling the likelihood with Markov Chain Monte Carlo (MCMC) methods would be more precise, but would greatly increase the computation time. Since the Fisher matrix is widely used in the literature, including the results we compare with, we also use the Fisher matrix formalism.

For the correlations C_{ij} and corresponding covariance **Cov**, the Fisher matrix is

$$\mathbf{F}_{\mu\nu} = \sum_{ij,kl} \frac{\partial C_{ij}}{\partial \mu} \mathbf{Cov}^{-1} \frac{\partial C_{kl}}{\partial \nu}, \tag{13}$$

where μ and ν are parameters and the two sums are over different correlations. If the observable does not enter the forecast, it is not included neither in the sums nor the covariance. One example of dropping observables is the removal of non-linear scales, as explained in the last subsection. The Cramer–Rao bound states that

$$\mathbf{F}_{\mu\mu}^{-1} \leq \sigma_\mu^2, \tag{14}$$

where $\mathbf{F}^{-1}$ denotes the Fisher matrix inverse and σ_μ^2 the expected parameter variance for the parameter μ. The covariance matrix of 2D correlations when assuming Gaussian fluctuations (Dodelson 2003) is

$$\mathbf{Cov}(C_{AB}, C_{DE}) = N^{-1}(l)(C_{AD}C_{BE} + C_{AE}C_{BD}), \tag{15}$$

where the number of modes is $N(l) = 2f_{Sky}(2l + 1)/\Delta l$, f_{Sky} is the survey fractional sky coverage and Δl is the band width (bin width in l).

Adding constraints from uncorrelated observables requires summing up the Fisher matrices. For example, the constraint of LSS/WL and cosmic microwave background (CMB) is

$$\mathbf{F}_{Combined} = \mathbf{F}_{LSS/WL} + \mathbf{F}_{CMB} \tag{16}$$

when assuming that the CMB is sufficiently uncorrelated with the LSS/WL experiment. This equation (16) can be proved using the covariance for two uncorrelated set of parameters is block diagonal

and equation (13) can be split in two parts. For the forecasts, all results (unless explicitly stated) add Planck priors.[4]

2.5 Figures of merit (FoMs)

FoMs are a simplified representation of the parameter constraints. A Fisher matrix of n parameters includes $n(n + 1)/2$ independent entries. Instead of including all the information on the errors and the covariance between parameters present in a covariance matrix, the FoM is only a single number. Comparing probes, effects and configurations are greatly simplified when using a single number. The FoMs let us study the gradual change with a parameter given on the x-axis, while adding different lines corresponding to various configurations. Also, the FoM is useful for comparing information along two dimensions in a table. While a single number does not fully capture the utility of a galaxy survey, but is a good measure to discuss trends.

The parameters included in the Fisher matrix forecast are

w_0, w_a, h, n_s, Ω_m, Ω_b, Ω_{DE}, σ_8, γ, galaxy bias,

where the first nine parameters equal the ones included in the dark energy task force (DETF) FoM (Albrecht et al. 2006). The galaxy bias (see Section 2.3) is parametrized with one parameter in each redshift bin for both galaxy populations. Fiducially, this study ignores the bias stochasticity, shear intrinsic alignments (Catelan, Kamionkowski & Blandford 2001; Hirata & Seljak 2004), uncertainties in photo-z distributions (Newman 2008; Matthews & Newman 2010) and other shear systematics (Bernstein 2009).

The DETF FoM is inversely proportional to the (w_0, w_a) 1σ contour area. Analogously Gaztañaga et al. (2012) defined an extended FoM,

$$\text{FoM}_S \equiv \frac{1}{\sqrt{\det\left[\mathbf{F}_S^{-1}\right]}}, \tag{17}$$

where S is a parameter sub-space. Parameters not in S are marginalized over. Since this concept is quite natural, other papers (e.g. Asorey et al. 2012; Kirk et al. 2013) define similar FoMs. Identical to Gaztañaga et al. (2012), we define three FoMs (in addition to DETF FoM).

(i) FoM_{DETF}. $S = (w_0, w_a)$. Dark energy task force (DETF) figure of merit. Inversely proportional to the error ellipse of (w_0, w_a).

(ii) FoM_w. $S = (w_0, w_a)$. Equivalent to FoM_{DETF}, but instead of $\gamma = 0.55$ from GR, the γ is considered a free parameter and is marginalized over.

(iii) FoM_γ. $S = (\gamma)$. Inverse error on the growth parameter γ, when marginalizing over the other cosmological parameters and the galaxy bias. Therefore, e.g. $\text{FoM}_\gamma = 10$, 100, respectively, corresponds to 10 per cent, 1 per cent expected error on γ.

(iv) $\text{FoM}_{w\gamma}$. $S = (w_0, w_a, \gamma)$. Combined figure of merit for w_0, w_a and γ. The 3D determinant also includes the correlation between the DE (w_0, w_a) and growth (γ) constraints.

Note that different authors introduce numerical prefactors of 1/4 (or $1/4\pi$) (Bridle & King 2007; Joachimi & Bridle 2010) in the FoM. In these papers, results are often presented in $\text{FoM}_{w\gamma}$, while the other FoMs are used to disentangle gains in measuring expansion

and growth history. One should be aware that the FoMs scale with area in the following way

$$\begin{aligned} \text{FoM}_w &\propto A \\ \text{FoM}_{DETF} &\propto A \\ \text{FoM}_\gamma &\propto A^{1/2} \\ \text{FoM}_{w\gamma} &\propto A^{3/2} \end{aligned} \tag{18}$$

when not including priors and A is the survey area. Including prior reduces the slope for small areas if the prior dominates. From numerical tests (not shown), the scaling above works well for the fiducial 14 000 sq. deg. survey.

2.6 Fiducial galaxy surveys

The two defined populations correspond to a spectroscopic (bright) and photometric (faint) survey. Both populations are magnitude limited, although a spectroscopic survey often would select specific targets to optimize the science return. The fiducial area is 14 000 sq. deg., which is around the expected sky coverage of stage-IV surveys.

Properties of the two populations are defined in the next two subsections, with Table 1 summarizing the central values. The shape of the galaxy distributions (not density) and also galaxy bias correspond exactly to the values in Gaztañaga et al. (2012). There the galaxy distributions were constructed by fitting a Smail type $n(z)$ (Efstathiou et al. 1991)

$$\frac{dN_F}{d\Omega dz} \propto A_F \left(\frac{z}{z_0}\right)^\alpha \exp\left(-\left(\frac{z}{z_0}\right)^\beta\right) \tag{19}$$

to the public COSMOS photo-z sample. In addition, the magnification (see Paper I) adds the term $\delta^{WL} = \alpha_s \delta_\kappa$, where κ is the convergence, to the galaxy counts overdensities. Fig. 1 specifies the fiducial magnification slopes (α_s).

Table 1. Parameters describing the two surveys/populations. The first section gives the area, magnitude limit, redshift range used in the forecast, redshift uncertainty modelled as a Gaussian, the redshift bin with and the resulting number of bins. In the second section is the galaxy bias ($\delta = b\delta_m$) and average galaxy shape uncertainty. The third section gives the galaxy density and parameters for the $n(z)$ shape.

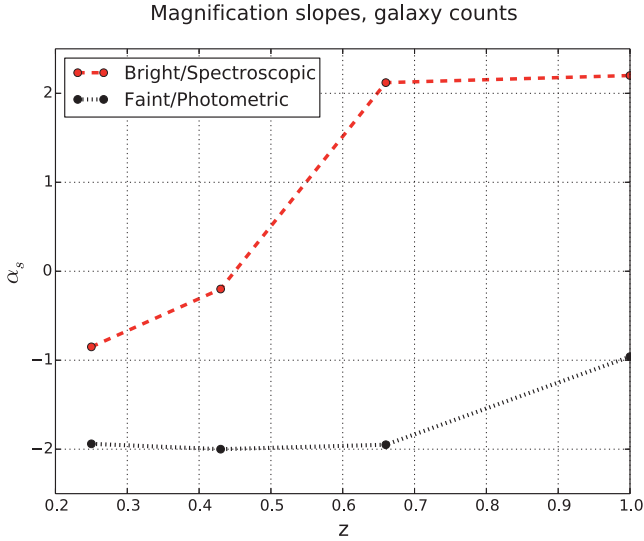| Parameter	Photometric (F)	Spectroscopic (B)
Area (sq. deg.)	14 000	14 000
Magnitude limit	$i_{AB} < 24.1$	$i_{AB} < 22.5$
Redshift range	$0.1 < z < 1.5$	$0.1 < z < 1.25$
Redshift uncertainty	$0.05(1 + z)$	$0.001(1 + z)$
z bin width	$0.07(1 + z)$	$0.01(1 + z)$
Number of bins	12	71
Bias: $b(z)$	$1.2 + 0.4(z - 0.5)$	$2 + 2(z - 0.5)$
Shape noise	0.2	No shapes
Density (galaxies arcmin^{-2})	6.5	0.4
$nz - z_0$	0.702	0.467
$nz - \alpha$	1.274	1.913
$nz - \beta$	2.628	1.083

Magnification slopes, galaxy counts

Figure 1. The number counts magnification slopes (α_s) for a bright ($18 < i_{AB} < =22.5$) and faint ($22.5 < i_{AB} < 24.1$) from the COSMOS sample. Values are extrapolated outside of this redshift range.

2.6.1 Bright/spectroscopic population

The bright population is defined by the flux limit $i_{AB} < 22.5$, has a Gaussian spectroscopic redshift uncertainty of $\sigma_{68} = 0.001(1 + z)$ and the galaxy density

$$\frac{dN_B}{d\Omega dz} = A_B \left(\frac{z}{0.702}\right)^{1.083} \exp\left(-\left(\frac{z}{0.702}\right)^{2.628}\right) \quad (20)$$

over $0.1 < z < 1.2$. Here A_B is a normalization amplitude and the fiducial density is 0.4 galaxies arcmin^{-2}, which is dense for a spectroscopic survey. The redshift evolution of the galaxy count bias is defined by

$$b_B(z) = 2 + 2(z - 0.5), \quad (21)$$

where $b(0) = 1$. To recover the radial information in the bright/spectroscopic sample, we use $\Delta z = 0.01(1 + z)$ narrow redshift bins.

2.6.2 Faint/photometric population

WL requires a dense and deep sample with imaging to measure galaxy shapes. The faint population resembles a wide-field lensing survey, magnitude limited to $i_{AB} < 24.1$ and $\sigma_{68} = 0.05(1 + z)$ Gaussian photo-z accuracy. This deeper magnitude selection gives the galaxy distribution:

$$\frac{dN_F}{d\Omega dz} = A_F \left(\frac{z}{0.467}\right)^{1.913} \exp\left(-\left(\frac{z}{0.467}\right)^{1.274}\right) \quad (22)$$

over $0.1 < z < 1.4$. The complete faint density is 17.5 galaxies arcmin^{-2}, and in addition we use only 50 per cent of the galaxies, which can either come from photo-z quality or shear measurement cuts. Similar to the spectroscopic sample, the bias model is linear with

$$b_F(z) = 1.2 + 0.4(z - 0.5) \quad (23)$$

which also has $b(0) = 1$. The faint sample uses $\Delta z = 0.07(1 + z)$ thick redshift bins and contributes strongest to the WL constraints. Decreasing the bin width would not improve the radial resolution or the RSD signal, as the photo-z error introduces an effective binning in redshift (Gaztañaga et al. 2012).

2.7 Observables

Table 2 defines the notation and also gives the observables included for a list of different cases. In this series of papers, the main topic is the combined constraints from photometric (F) and spectroscopic (B) surveys, either alone (F or B) or for overlapping (F×B) or non-overlapping (F+B) areas. The 'All' notation means both shear and galaxy counts, while 'Counts' includes only counts. Part of the benefit of overlapping surveys comes from additional cross-correlations. To quantify their impact, the second part of the table therefore presents the notation for removing selected cross-correlations. Table 3 contains a list of cross-correlations which enter both directly in the text and Table 2.

3 RESULTS

In this section, we investigate the combined constraint from galaxy counts and shear, treating each survey as a separate galaxy

Table 2. Summary of the probe combinations and the correlations included. The first column is the notation, the second column gives the correlations included and the third column is a short description. Each row corresponds to a different probe combination. The first block shows standard combinations, the second block shows combinations removing counts–shear correlations and the third block includes probes without cross-correlations of the two samples. Here 'Counts' includes only galaxy counts, while 'All' also includes shear. The observables $\langle \gamma_B \gamma_F \rangle$ and $\langle \delta_F \gamma_B \rangle$ are also included, but not listed as their contributions are minor.

Notation	Observables	Description
F:All	$\langle \delta_F \delta_F \rangle + \langle \delta_F \gamma_F \rangle + \langle \gamma_F \gamma_F \rangle$	Faint population
B:All	$\langle \delta_B \delta_B \rangle + \langle \delta_B \gamma_B \rangle + \langle \gamma_B \gamma_B \rangle$	Bright population
F×B:All	F+B:All $+ \langle \delta_F \delta_B \rangle + \langle \delta_B \gamma_F \rangle$	Overlapping faint and bright
F+B:All	F:All + B:All $- \langle \gamma_B \gamma_B \rangle$	Non-overlapping faint and bright
F×B$-\langle \delta_B \gamma_B \rangle$:All	F:All + B:All $+ \langle \delta_B \delta_F \rangle$	F×B-All removing $\langle \delta_B \gamma_F \rangle$
F×B$-\langle \delta_F \gamma_F \rangle$:All	B:All $+ \langle \delta_F \delta_F \rangle + \langle \gamma_F \gamma_F \rangle + \langle \delta_F \delta_B \rangle + \langle \delta_B \gamma_F \rangle$	F×B-All removing $\langle \delta_F \gamma_F \rangle$
F×B$-\langle \delta \gamma \rangle$:All	B:Counts + F:Counts $+ \langle \gamma_B \gamma_B \rangle + \langle \gamma_F \gamma_F \rangle$	F×B-All, removing all cross-correlation of counts and shear
F×B$-\langle FB \rangle$:Counts	$\langle \delta_B \delta_B \rangle + \langle \delta_F \delta_F \rangle$	F×B-Counts, removing the bright–faint cross-correlations of counts
F×B$-\langle FB \rangle$:All	F:All + B:All	F×B-All, removing all the bright–faint cross-correlations, i.e. $\langle \delta_F \delta_B \rangle$ and $\langle \delta_B \gamma_F \rangle$. Equivalent to F+B:All with covariance between F and B.

Table 3. Notation for different cross-correlations. First column gives the cross-correlation and the second column is a short description.

Notation	Description
$\langle \delta_F \delta_B \rangle$	Counts–counts cross-correlations of the two galaxy populations. Important for sample variance cancellation.
$\langle \delta_B \gamma_F \rangle$	Counts–shear cross-correlations of foreground spectroscopic galaxy counts and shear.
$\langle \gamma_B \gamma_B \rangle$	Shear–shear for the bright galaxies. In overlapping surveys, the bright galaxies are a subset of the photometric survey. This term is of minor importance since the bright sample is shallower and less dense.

population. The first five subsections compare how different effects such as RSD, BAO, lensing and intrinsic correlations contribute to the forecast. In the last subsection, we present the main forecast table and discuss the relative contribution of each effect and the impact with overlapping photometric and spectroscopic surveys. Lastly, we look at the effect of magnification. Contour plots can be found in Appendix B.

3.1 Auto- versus cross-correlations

This subsection studies how the galaxy clustering and lensing observables affect the forecast. The significant correlations for close redshift bins are the shear–shear $\langle \gamma \gamma \rangle$ and counts–counts $\langle \delta \delta \rangle$ correlations. Here the counts–counts correlation of the spectroscopic sample includes a strong RSD signal and intrinsic cross-correlation between nearby redshift bins. For large redshift bin separation, the counts–shear $\langle \delta \gamma \rangle$ cross-correlations are the strongest. To separate the contribution from different cross-correlations, we introduce the variable ΔZ_{Max}. All correlations C_{ij} are required to satisfy

$$|z_j - z_i| \leq \Delta Z_{\mathrm{Max}}, \tag{24}$$

where z_i, z_j, respectively, are the mean of redshift bins i and j. This requirement applies only when specified for the figures. Which cross-correlations enter is discussed together with the forecast results in the next paragraphs.

The auto-correlations are always included from the ΔZ_{Max} definition, which for probes with lensing includes the shear–shear auto-correlations. In Fig. 2, this shows at $\Delta Z_{\mathrm{Max}} = 0$ as a gap between lines which includes shear (All) or not (Counts). The lensing with its broad kernel can be seen to better measure DE (top panel, also includes γ) than the growth of structure (bottom panel). Overall, galaxy shear leads to four to five times improvement for the combined figure of merit (FoM$_{w\gamma}$). In the region $0.01 < \Delta Z_{\mathrm{Max}} < 0.1$, the forecast also includes cross-correlations between bright/spectroscopic redshift bins, with a significant jump when including the cross-correlation with the adjacent bin. These cross-correlations contribute significantly and are studied in later subsections in the context of the Limber approximation (3.2), RSD (3.4) and BAO (3.5).

The F×B−$\langle \delta \gamma \rangle$ lines are the forecast of F×B:All without counts–shear correlations. At larger ΔZ_{Max}, the counts–shear lensing becomes important, which can be seen from F×B:All and F+B:All having higher FoM$_{w\gamma}$ than F×B−$\langle \delta \gamma \rangle$. Note that higher ΔZ_{Max} also includes shear–shear tomography, which also enters in F×B−$\langle \delta \gamma \rangle$. Another lensing effect is the magnification of the galaxy counts (Paper I). Intrinsic clustering dominates the counts–counts signal at low redshift separation, while magnification only becomes important at higher separations where the intrinsic corre-
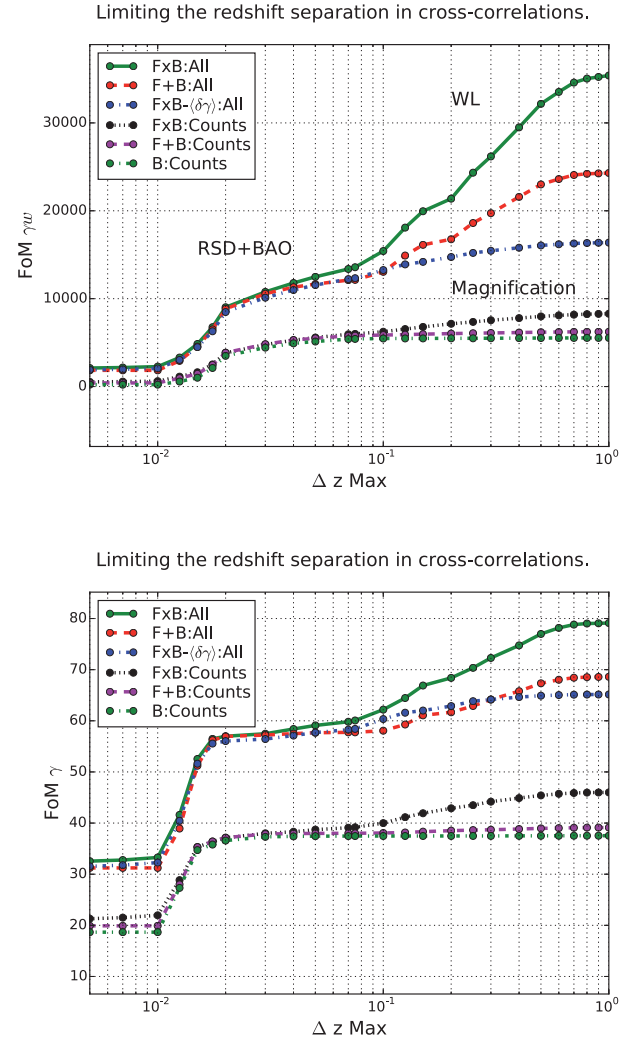

Figure 2. The FoM dependence on the maximum redshift separation for cross-correlations included in the forecast (ΔZ_{Max}). Lines correspond to the probes F×B:All, F+B:All, F×B−$\langle \delta \gamma \rangle$:All, F×B:Counts, F+B:Counts and B:Counts. The top and bottom panels, respectively, correspond to FoM$_{w\gamma}$ and FoM$_{\gamma}$.

tion also vanishes. The separation of F×B:Counts and F+B:Counts at high ΔZ_{Max} is due to magnification. Magnification is also included in F and B, but the impact is strongest for the combined overlapping samples. In Section 3.7, we study the effect of magnification when the surveys include both galaxy counts and shear.

Fig. 3 shows the FoM normalized to FoM($\Delta Z_{\mathrm{Max}} = 1$) = 1, where the gain has saturated. The same information is already presented (Fig. 2), but these plots are better to discuss the relative contribution of different correlations. In FoM$_{w\gamma}$ (top panel), there is large spread between the lines. For B:Counts mostly close ($\Delta Z_{\mathrm{Max}} < 0.1$) correlations are important. When including magnification (F×B:Counts) or the shear–shear tomography (F×B−$\langle \delta \gamma \rangle$), there is some more benefit from cross-correlations of widely separated redshift bins. The bottom lines are F×B:All and F+B:All where counts–shear contribute significantly and many different correlation types contribute to the constraints. There is much less difference for FoM$_{\gamma}$ (bottom panel), where the auto-correlations account for 40–50 per cent for all probes. For B:Counts, the intrinsic counts–counts correlation between bins provides the rest, while F×B:All has a 25 per cent contribution from counts–shear lensing.
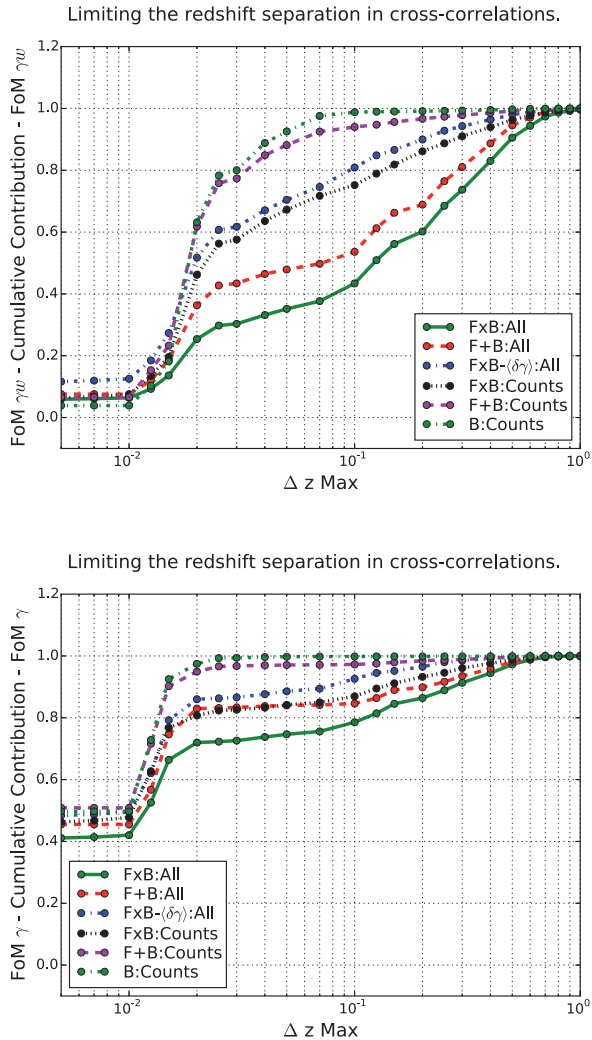
Limiting the redshift separation in cross-correlations.

Limiting the redshift separation in cross-correlations.

Figure 4. Normalized cumulative FoM contributions for different probes. The x-axis is ΔZ_{Max} and the FoMs are normalized by $\text{FoM}(\Delta Z_{\text{Max}} = 1) = 1$. All results are for F×B:All and the lines correspond to FoM_γ, FoM_{DETF}, FoM_w and $\text{FoM}_{w\gamma}$.

Limiting the redshift separation in cross-correlations.

Figure 3. Normalized cumulative FoM contributions for different probes. The x-axis is ΔZ_{Max} and the FoMs are normalized by $\text{FoM}(\Delta Z_{\text{Max}} = 1) = 1$. Each line is a probe and the two panels show the result for different FoMs.

Fig. 4 is similar to Fig. 3, but compares the normalized cumulative constraints of F×B:All for the different FoMs: FoM_γ, FoM_{DETF}, FoM_w and $\text{FoM}_{w\gamma}$ in the same plot. The FoM_γ line depends strongly on the auto-correlation. This is expected as the galaxy clustering (counts–counts) is important for measuring the growth. Interestingly, the next two lines are FoM_{DETF} and FoM_w, while $\text{FoM}_{w\gamma}$ which includes both DE and the growth (γ) benefits the most from different correlations. Also, fixing the bias changes the correlations that contribute (plot not shown), while keeping the FoM/line order. How marginalizing over the bias changes the forecast is an important part of this paper and is studied further in Paper III.

3.2 Limber approximation

Paper I compared the correlations estimated using the exact calculations to the correlations when using the Limber approximation. For narrow redshift bins of $\Delta z = 0.01(1 + z)$, the Limber approximation can overestimate the galaxy counts auto-correlations by a factor of 2–3 (Paper I, fig. 8). Further, in the Limber approximation there is no counts–counts cross-correlations between non-overlapping redshift
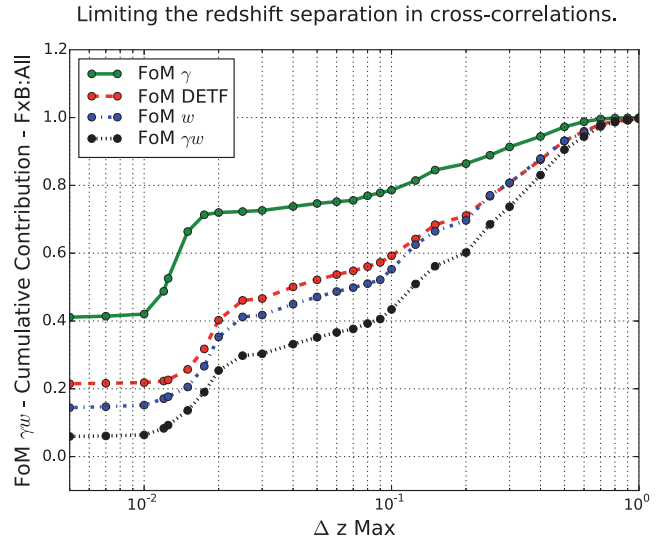
bins, which is not a good approximation for $\Delta z = 0.01(1 + z)$-wide bins in the bright sample.

Fig. 5 compares the exact calculations with the Limber approximation. Included in the panels is one line showing the exact calculations with RSD, while the other two lines are the exact calculation and Limber approximation in real space (No RSD). The RSD signal in the correlation is powerful, especially in measuring γ. Comparing the three lines shows how cross-correlations and RSD contribute to measuring DE and the growth of structure. For γ including the cross-correlations has little effect, while the RSD improves FoM_γ for F×B:All by 70 per cent. On the other hand, for FoM_{DETF} the cross-correlation of galaxy count in the radial direction is powerful, while the RSD signal contributes little. One can understand the main traits from the amplitudes and shapes of the correlations. The γ parameter changes the clustering amplitude, while DE parameter ω more directly affects the shape.

For FoM_{DETF} without RSD (real space), the exact calculations and Limber approximation results cross around $\Delta Z_{\text{Max}} = 0.015$. The width of the spectroscopic redshift bins here is $\Delta z = 0.01(1 + z)$ and around the crossing the exact calculations begin to include correlations with nearby redshift bins. These are important for DE constraints (Section 3.5). Also, similar to FoM_γ, when counts–shear becomes important at large ΔZ_{Max}, the difference decreases because of the smaller error in Limber approximation.

The higher galaxy counts auto-correlations in the Limber approximation reduce the impact of shot noise. One can see in Fig. 5 how the FoM_γ line in the top panel of Fig. 5 is slightly lower for the exact calculation than the Limber approximation. For larger ΔZ_{Max}, the lines first diverge before converging when also including counts–shear cross-correlations (high ΔZ_{Max}). While the Limber approximation is accurate for the counts–shear signal, the higher galaxy counts lead to an overestimated error (see equation 15). As a result, the counts–shear correlations contribute less in the Limber approximation.

Comparing the Exact correlations and the Limber approximation.
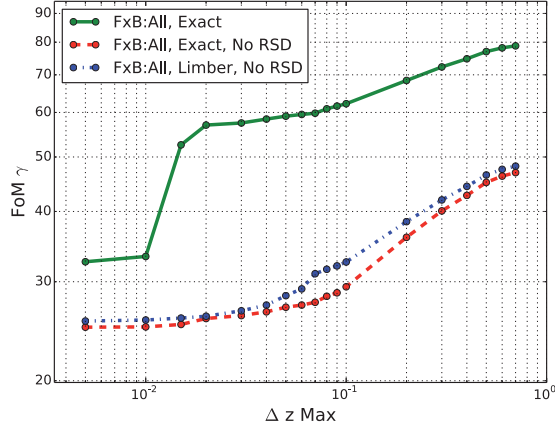
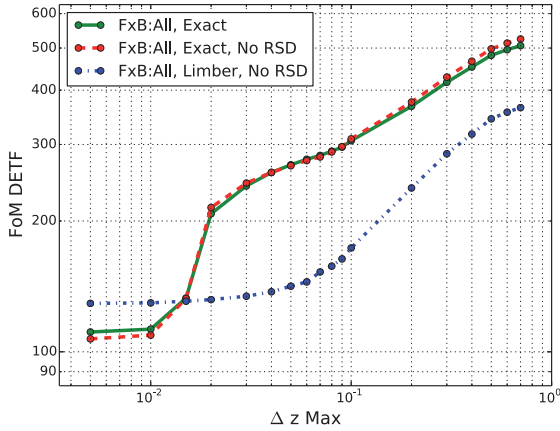Comparing the Exact correlations and the Limber approximation.

Figure 5. Forecast for F×B:All using the exact calculations and the Limber approximation. The first two lines, respectively, show the FoM in redshift and real space, while the last uses the Limber approximation in real space. The top and bottom panels, respectively, show FoM_γ and FoM_{DETF}.

3.3 Resolution in redshift

Increasing the number of spectroscopic bins results in better constraints. The redshift bin width in a 2D forecast corresponds approximately to the maximum scale $k_{\max} = 2\pi/\lambda_{\min}$, where $\lambda_{\min}$ is the comoving width of the redshift bins (Asorey et al. 2012). The gain for small enough bins when increasing the number of bins therefore mainly comes from probing smaller scales. Note that having such a large number of bins can lead to including more non-linear modes in the radial direction than in the angular direction. To be consistent, we need to limit the number of radial bins to the corresponding $l_{\max}$ scale (see Asorey et al. 2012; Asorey, Crocce & Gaztañaga 2014). In our case, Nz 70 is the corresponding number and in this regime PAUz is quite close to spec-z. In this section, we are not comparing to a 3D forecast, but focusing on the effect of the covariance between the observables.

Fig. 6 shows $\text{FoM}_{w\gamma}$ for an increasing number of bins, where the bin width $\Delta_z = w(1 + z)$ is set by the number of redshift bins.[5] Focusing first on the result for many redshift bins, one expects the

[5] Let z_i denote the edges between redshift bins and where z_0 is the start of the redshift range. A frequently used redshift binning is

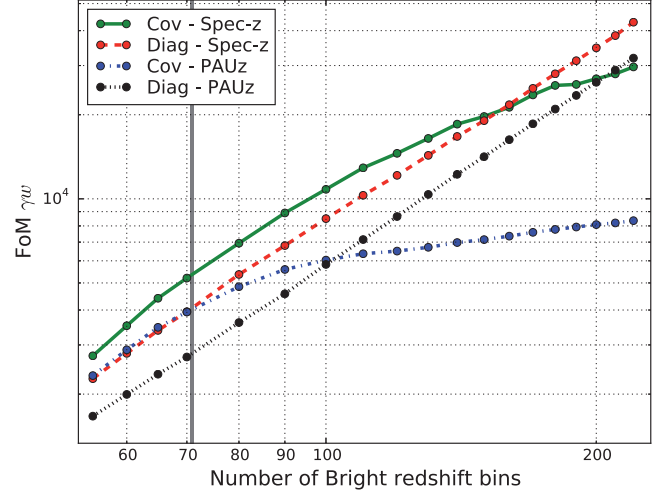Effect of covariance for the Bright/spectroscopic sample.

Figure 6. Effect of the covariance and photo-z. The lines all show $\text{FoM}_{w\gamma}$ for galaxy counts for the spectroscopic sample, with the number of bins varying on the x-axis. Two lines (cov) include the full covariance, while the other two (only diag) use only the variance. Each of these configurations is run using either spectroscopic redshifts (spec-z) or narrow-band photometry (PAUz, $\sigma_{68}/(1 + z) = 0.0035$). A vertical line marks the fiducial number of spectroscopic redshift bins (71).

covariance to be important for increasingly thinner bins. The galaxy density per bin also decreases, but the fiducial sample is dense (0.4 galaxies arcmin^{-2}) and the effect of shot noise is less important (plot not shown). Assume that the auto-correlations are close to equal in two bins ($C_{AA} \approx C_{BB}$) and define $\alpha \equiv C_{AB}/C_{AA}$. The Pearson correlations, $R[A, B] = \text{Cov}(A, B)/\sqrt{\text{Var}[A] * \text{Var}[B]}$, for the covariance matrix (equation 15) are then

$$R[\text{Auto}(AA), \text{Auto}(BB)] \approx \alpha^2 \tag{27}$$

$$R[\text{Auto}(AA), \text{Cross}(AB)] \approx \alpha\sqrt{2}/\sqrt{1 + \alpha} \tag{28}$$

when ignoring the shot noise. From these equations, the covariance increases for thinner bins which have higher α (see Paper I). The largest covariance is not between auto-correlations, but between the auto- and cross-correlations. Previous studies expected the covariance to saturate the result, but could not demonstrate this due to technical difficulties with many bins[6] (Asorey et al. 2012; Di Dio et al. 2013). In Fig. 6, the covariance limits the results, with the lines being even flatter (and numerical unstable) when approaching 300 bins. The forecast also saturates for FoM_w, FoM_γ and FoM_{DETF} (not

$z_n = z_{n-1} + (1 + z_{n-1}) * w$, where the constant w gives the bin width. Provable by mathematical induction, then

$$z_n = (1 + z_0)(1 + w)^n - 1 \tag{25}$$

is the nth edge between the redshift bin. For a binning $\Delta_z = w(1 + z)$, then

$$w = \sqrt[N]{\frac{1 + z_{\text{Max}}}{1 + z_0}} - 1 \tag{26}$$

divides the interval $[z_0, z_{\text{Max}}]$ in n bins into N redshift bins.

[6] In this subsection, the forecast excludes all counts–counts cross-correlations C_{ij} with $0.1 < |z_j - z_i|$ for redshift bins i, j. These include little cosmological information (for magnification, see Section 3.7), and removing these helps to reduce the dimension of the covariance matrix.
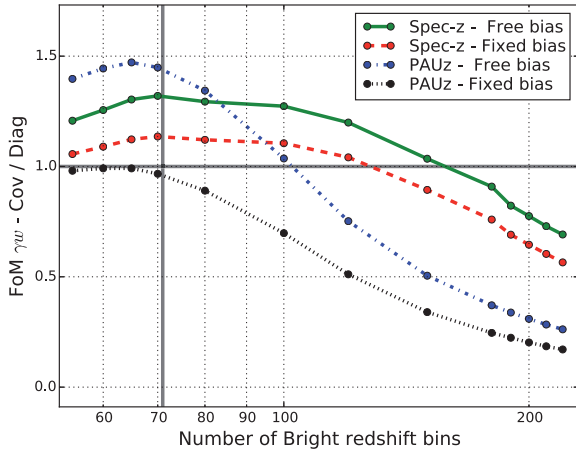
Figure 7. The gain from the covariance. This figure shows the forecast ratio between including the full covariance and only the diagonal entries. All lines show FoM$_{w\gamma}$ for the bright sample using galaxy counts (B:Counts) as a function of redshift bins. Two lines use a spectroscopic sample (spec-z), while the other two use narrow-band photo-z sample (PAUz). For two lines, we marginalize over the bias (free bias), while for the other two the bias is fixed (fixed bias). A vertical line marks the fiducial number of spectroscopic redshift bins (71).
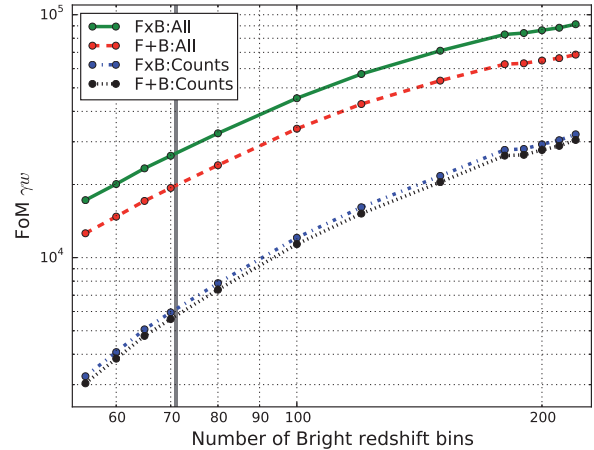

Figure 8. The forecast for different probes and increasing number of bins. On the x-axis is the number of spectroscopic redshift bins, while the lines show FoM$_{w\gamma}$ for the probe combinations F×B:All, F+B:All, F×B:Counts and F+B:Counts. A vertical line marks the fiducial number of spectroscopic redshift bins (71).

shown). For PAUz the forecast FoMs become flat earlier (less bins), since the photo-z also correlates the fluctuations in the different redshift bins.

For an intermediate low number of bins (50–100), the covariance between observables increases FoM$_{w\gamma}$. This result is counterintuitive, but is similar to the sample variance cancellations for multiple galaxy tracers. When two observables depend differently on nuisance parameters (e.g. bias), the covariance between the observables introduces a covariance between the nuisance parameters. The additional covariance between the bias parameters reduces their freedom, which increases cosmological constraints when marginalized over. The covariance naturally also reduces the information, since the observables are no longer independent. If the forecast improves or degrades depends on the details of these competing effects (see Eriksen & Gaztañaga 2014).

Fig. 7 shows the FoM$_{w\gamma}$ ratio between including the full covariance and only the diagonal entries (variance). For spectroscopic redshifts and marginalizing over the bias (free bias), the covariance increases FoM$_{w\gamma}$ until about 160 spectroscopic bins. This shows that the covariance between different redshift slices increases constraints through reducing the sample variance. When fixing the bias, the gain is about three times lower, but it is still a 10 per cent effect. We attribute this to a changed covariance between the cosmological parameters, some of which we marginalize over. While the constraints can be higher for only the variance, the covariance should be included in parameter fits to not bias the results. With narrowband photo-z (PAUz), the effect of the covariance changes. For a free bias the gain is higher, while there is no benefit when fixing the bias.

How does the same-sky (F×B/F+B) conclusions depend on the number of spectroscopic bins? Fig. 8 shows the combined forecast (F×B, F+B) for the fiducial case, which uses spectroscopic redshift and includes the covariance. The bright sample (Fig. 8) benefits from more redshift bins. This however also increases the number of counts–counts cross-correlations with the photometric sample and cross-correlations of spectroscopic galaxy counts with shear. For

both 'All' and 'Counts', the F×B/F+B ratio is nearly constant over a large number of spectroscopic redshift bins. This shows that our conclusions on the same-sky issue are quite robust with respect to the number of redshift bins.

3.4 Redshift space distortions (RSD)

RSD affects the overdensities of galaxies. A matter overdensity attracts galaxies, which change their velocities and introduce a change in redshift. At linear level, the change in galaxy count overdensities is the Kaiser effect. The redshift space galaxy spectrum $\tilde{P}_{\mathrm{Gal}}(k)$ is then

$$\tilde{P}_{\mathrm{Gal}}(k, \mu) = (b + \mu^2 f)^2 P(k), \tag{29}$$

where $P(k)$ is the real space matter power spectrum, b is the galaxy bias, μ is the cosine of line of sight angle and $f \equiv \Omega_{\mathrm{m}}(z)^\gamma$. In the forecast, the RSD effect enters in the 2D correlations. Overdense regions attract nearby galaxies, which can move galaxies between redshift bins. This effect often increases the amplitude of the 2D correlations (see Paper I).

The RSD is a powerful effect for measuring γ. Fig. 9 shows how including RSD in the correlations improves FoM$_\gamma$ by a factor of between 1.5 and a few. For the other FoMs (not shown), RSD decreases the result with 0–5 per cent. Now we first focus on the results for counts. Observing galaxy counts over separate skies (F+B:Counts) is the combination which benefits most from RSD. For only B:Counts (not shown), the RSD improves for the fiducial binning the constraints with a factor of 3.9. The added RSD component is independent of bias, and therefore reduces the degeneracies between γ and the bias. In F×B:Counts, the surveys are overlapping and the samples (F and B) can be cross-correlated. The cross-correlations and also sample variance cancellation directly from overlapping volumes (Section 3.6) improve bias constraints, and RSD is therefore less important for F×B:Counts.

One should note that comparing models with and without RSD in the angular correlations is slightly misleading. The forecast in redshift space or real space includes the same correlations and only differ by including the RSD component in the correlations. One can therefore not assume that RSD always improves the parameter
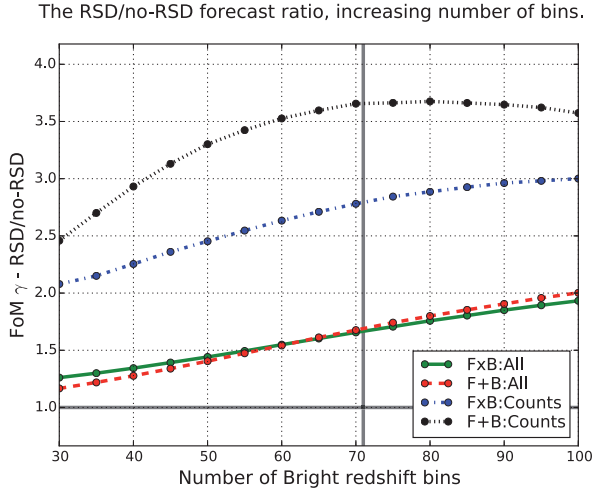
Figure 9. The FoM$_\gamma$ ratio between a redshift and real space forecast when varying the number of spectroscopic redshift bins. A vertical line marks the fiducial number of spectroscopic redshift bins (71). The four lines correspond to F×B:All, F+B:All, F×B:Counts and F+B:Counts.

constraint, but the benefit depends largely on the resulting correlations between the parameters. As seen in the last paragraph, the measurement of γ improves greatly from RSD. On the other hand, in the theoretical real space angular correlations, there is radial information in the cross-correlations between redshift bins. Including RSD will, as we will see, reduce the DE constraints from intrinsic galaxy counts cross-correlations with nearby redshift bins.

When including shear, the importance of RSD naturally decreases (Fig. 9, F×B:All and F+B:All). These probes also include the shear–shear signal, which is unaffected by the RSD. Even if the ratios are lower, the factor of 2 is still a good improvement. Since F+B:Counts benefit more than F×B:Counts from RSD, the separation between F+B:All and F×B:All is smaller than expected. One can understand this from looking at the counts–shear variance. The variance for the cross-correlation of a foreground galaxy counts (δ_i) density with background shear (γ) is (see equation 15)
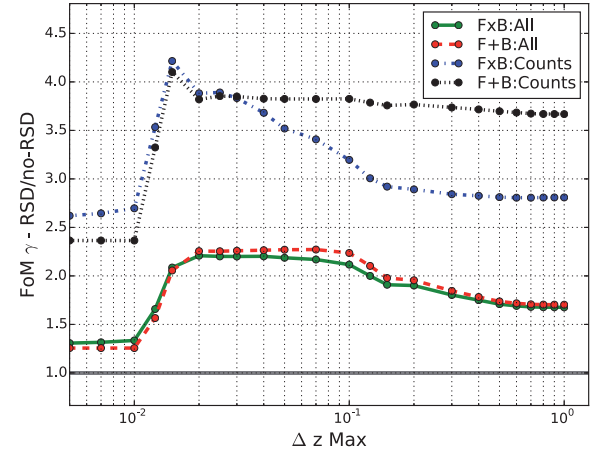
$$\text{Var}(\langle \delta_i \gamma \rangle) = N^{-1}(l)[\langle \delta_i \delta_i \rangle \langle \gamma \gamma \rangle + \langle \delta_i \gamma \rangle^2], \qquad (30)$$

where $N(l)$ is the number of modes. The $\langle \delta_i \gamma \rangle$ signal and the second term in the variance are approximately independent of RSD. On the other hand, the $\langle \delta_i \delta_i \rangle$ auto-correlations increase strongly from RSD. Since the error increases, including RSD in the forecast reduces the importance of counts–shear.

The top panel of Fig. 10 shows how including RSD affects the forecasts. Instead of studying the FoMs as a function of number of redshift bins, this figure uses the fiducial binning and ΔZ_{Max} is varied. Section 3.1 explained how ΔZ_{Max} can be used to distinguish between contributions from auto-correlations, cross-correlations with nearby redshift and counts–shear WL. The largest RSD effect is for FoM$_\gamma$, and F+B:Counts increase by a factor of 3.6 with respect to the real space forecast. When including cross-correlations between nearby bins, the importance of RSD increases for all probe combinations. In Paper I, we showed how RSD affects the auto- and cross-correlations differently, which here improve the growth constraints. For F×B:Counts, higher ΔZ_{Max} also includes WL magnification. Magnification adds an additional bias measurement, therefore decreasing the impact of RSD.

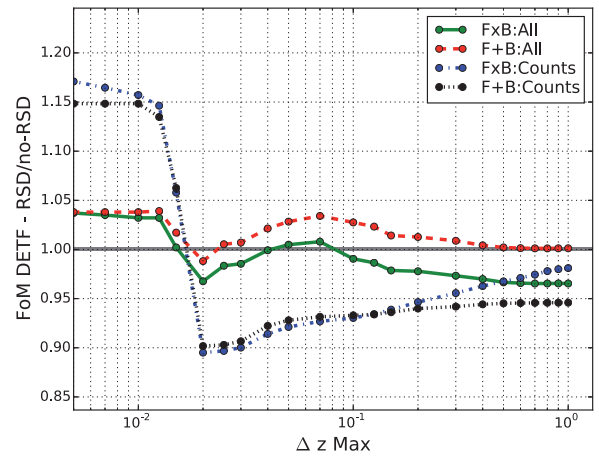Lastly, the FoM$_{\text{DETF}}$ (Fig. 10, bottom panel) includes some interesting trends. For the auto-correlation, the RSD improves the

Figure 10. FoM ratio between redshift and real space when varying the largest redshift separations in the cross-correlations (ΔZ_{Max}). In the two plots corresponding to FoM$_\gamma$ and FoM$_{\text{DETF}}$, the four lines are the probes F×B:All, F+B:All, F×B:Counts and F+B:Counts.

DE constraints. Around $0.01 < \Delta Z_{\text{Max}} < 0.02$, the forecast also includes galaxy counts cross-correlations between spectroscopic redshift bins. Then the FoM$_{\text{DETF}}$ ratio suddenly drops because the RSD suppresses the cross-correlation with nearby redshift bins, which are important for DE constraints. Since F×B:Counts depend strongly than F+B:Counts on magnification, the lines separate at high ΔZ_{Max}. The magnification signal, which has similar covariance to counts–shear and benefit from RSD reducing amplitude of the auto-correlations. Since F×B:Counts depends strongly on magnification than F+B:Counts, the lines separate at high ΔZ_{Max}.

3.5 Baryon acoustic oscillation (BAO)

In the observed galaxy distribution, BAO is a characteristic scale (~150 Mpc today), which is measurable both in the transverse/angular and radial/redshift direction (Gaztañaga, Cabré & Hui 2009; Reid et al. 2012). Observing the BAO can therefore probe cosmology by measuring the comoving and angular diameter distance. Accurate prediction of the power spectrum is done by solving the Boltzmann equation. The Eisenstein–Hu analytical power spectrum formula we use here is less accurate, but can be used to estimate
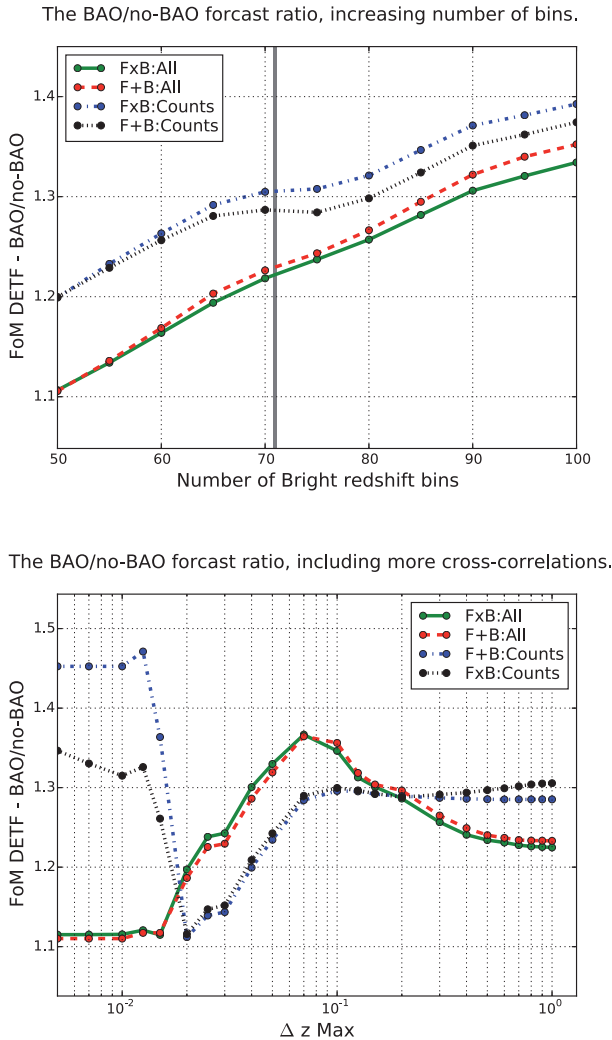
The BAO/no-BAO forcast ratio, increasing number of bins.

The BAO/no-BAO forcast ratio, including more cross-correlations.

Figure 11. Effect of including BAO wiggles. The ratio divides the fiducial forecast on one removing the BAO wiggles in the Eisenstein–Hu power spectrum. In the top and bottom panels, the FoM$_{\rm DETF}$ is, respectively, shown when varying the number of spectroscopic redshift bins and $\Delta Z_{\rm Max}$. The four lines are for the probes F×B:All, F+B:All, F×B:Counts and F+B:Counts. A vertical line in the upper panel corresponds to the fiducial number of spectroscopic redshift bins (71).

the power spectrum both only with the continuum and including the BAO wiggles. In this subsection, we compare the forecasts with and without the BAO feature.

Fig. 11 shows in the top panel the ratio between including and not the BAO (BAO/no-BAO) for different numbers of spectroscopic redshift bins. For the fiducial binning (71 bins), the FoM$_{\rm DETF}$ improves with 20–30 per cent, while FoM$_\gamma$ only changes with ±2 per cent (not shown). This trend is opposite to RSD, discussed in Section 3.4, where RSD contributed strongly to γ constraints (FoM$_\gamma$), but only gave minor changes to the DE constraints (FoM$_{\rm DETF}$). Measuring γ depends on measuring the amplitude, while the DE constraints come more from the power spectrum shape measurements (BAO position as opposed to amplitude). The RSD breaks the degeneracy between the galaxy bias and the growth parameter (γ). On the other hand, the BAO introduces a known distance scale, which is more suited to measure the shape and expansion history.

The BAO peak can in configuration space be modelled by a 30 Mpc h^{-1} wide Gaussian. For the fiducial binning (71 bins), the bin width at $z = 0.5$ is 35 Mpc h^{-1}. When increasing the number of bins, one decreases the redshift bin width, which leads to a more precise location of the BAO peak. Thinner bins can also, as we will discuss, better measure the radial BAO in the cross-correlations between nearby bins. As a result, we find the FoM$_{\rm DETF}$ BAO/no-BAO ratio to around double when using 100 instead of 71 bins in the spectroscopic sample.

Fig. 11, bottom panel, shows the BAO/no-BAO ratio when increasing $\Delta Z_{\rm Max}$. The forecast includes only auto-correlations when $\Delta Z_{\rm Max} = 0$, while $0.01 \leq \Delta Z_{\rm Max}$ also has the cross-correlations between redshift bins. For only auto-correlations of galaxy counts, the ratio is artificially high since the forecast uses one bias parameter per redshift bin and population. The 'Counts' ratio therefore drops when including the cross-correlations between close redshift bins. Previously, Paper I found a stronger BAO signal in the cross-correlation between nearby bins than in the auto-correlation. This was caused by the cross-correlation selecting galaxy pairs with a given radial distance, therefore suppressing the small-scale information. For both 'All' and 'Counts', the BAO/no-BAO ratio grows from 1.1 to 1.3–1.35, showing that radial BAO is an important contribution.

The shear–shear auto-correlations are in 'All' included for all $\Delta Z_{\rm Max}$ values. When including lensing, the BAO/no-BAO ratio increase is higher with $\Delta Z_{\rm Max}$, since the BAO helps to break degeneracies. For higher $0.1 < \Delta Z_{\rm Max}$, counts–shear becomes important and the ratio again decreases. Since the ratio also decreases for a fixed bias (not shown), the decrease does not result from count–shear providing an additional bias measurement, but from the counts–shear signal depending more weakly on BAO. Because the galaxy counts magnification is a weak effect (see Section 3.7), the lines for only counts remain quite flat for $\Delta Z_{\rm Max} > 0.1$.

3.6 Combining WL, RSD and BAO

Previous subsections studied in detail the separate benefits of the covariance, RSD, WL and BAO. This subsection builds on those and compares the relative impact of each physical effect, including knowledge of galaxy bias and sample variance cancellations. The main results are presented in two Tables, corresponding to FoM$_{w\gamma}$, FoM$_\gamma$, FoM$_{\rm DETF}$ and FoM$_w$. For layout reasons, FoM$_{w\gamma}$ and FoM$_\gamma$ are shown in Table 4, while FoM$_{\rm DETF}$ and FoM$_w$ are included in Table 5. Each row corresponds to a different probe and dashed lines divide the rows into five sections. The first two sections quantify the benefit of overlapping photometric and spectroscopic galaxy surveys. In the third section, we study the single population, while the fourth and fifth sections present special cases (see Table 2). In the columns are the forecast for a free/fixed galaxy bias and when removing different effects.

The first three rows of Table 4 show the forecast for F×B:All, F+B:All and the same-sky benefit: F×B/F+B. For FoM$_{w\gamma}$ we find a 50 per cent same-sky gain, which corresponds to 30 per cent increase in area (equation 18). The origin of this benefit in FoM$_{w\gamma}$ is explained in a companion paper (Eriksen & Gaztañaga 2014). Here we focus on describing the different results in detail. In the DE FoMs (FoM$_w$ and FoM$_{\rm DETF}$) the benefit is similar, while the FoM$_\gamma$ ratio is 1.1, which corresponds to a 20 per cent larger area. While the details differ, for galaxy counts and shear we find similar benefits from overlapping photometric and spectroscopic surveys. In general, the absolute numbers in the forecast presented depend strongly on the parametrization of the galaxy bias. For example,

Table 4. Comparison of different combinations of observables and effects. The two tabulars correspond to $\mathrm{FoM}_{w\gamma}$ and FoM_γ indicated in the upper-left corner. The label column indicates the populations in the rows (B:bright/spectroscopic, F:faint/photometric) and using overlapping ($\times$) or separate ($-$) skies. 'Counts' includes only overdensities of number counts, while 'All' also includes galaxy shear. The rows are divided through dashed lines into five sections. First two sections study overlapping versus non-overlapping surveys, where the last line is the fraction gained using overlapping surveys. Third row section presents the single population cases (F or B). The fourth section looks at special cases, defined in Section 2.7, designed to understand which correlations contribute most. Fifth section is the forecast for overlapping surveys without any cross-correlations and the ratio to non-overlapping surveys. The column 'Fiducial' is the fiducial forecast, while 'xBias' fixes the galaxy bias. In the next columns are forecasts corresponding to removing magnification (No Magn), weak lensing (No WL), redshift space distortions (No RSD) and baryon acoustic oscillations (No BAO). The last three columns include fixed bias cases.

10^{-3} FoM γw	Fiducial	xBias	No Magn	No WL	No RSD	No BAO	No WL-xBias	No RSD-xBias	No BAO-xBias
F×B:All	35.5	213	35.1	7.32	17.1	27.8	59.1	163	206
F+B:All	24.3	193	24.2	6.13	11.0	18.0	61.5	155	183
Improvement	1.5	1.1	1.4	1.2	1.6	1.6	0.96	1.1	1.1
F×B:Counts	8.29	61.9	7.32	7.32	3.31	6.00	59.1	50.2	48.0
F+B:Counts	6.24	62.0	6.13	6.13	1.72	4.41	61.5	53.2	44.6
Improvement	1.3	1.00	1.2	1.2	1.9	1.4	0.96	0.94	1.1
F:All	3.10	51.2	3.07	0.064	2.61	2.77	2.68	52.0	53.2
B:All	7.91	52.6	7.91	5530	2.76	5.42	45.4	42.6	43.1
F:Counts	0.077	2.85	0.064	0.064	0.036	0.050	2.68	2.93	2.34
B:Counts	5.53	45.4	5530	5.53	1.45	3.78	45.4	37.9	31.6
F×B−⟨$\delta_F\gamma_F$⟩:All	32.4	201	32.3	7.32	15.4	25.3	59.1	152	194
F×B−⟨$\delta_B\gamma_F$⟩:All	33.8	208	33.4	7.32	16.2	26.3	59.1	160	201
F×B−⟨$\delta\gamma$⟩:All	16.4	100	16.1	7.32	7.46	12.0	59.1	79.2	89.6
F×B−⟨FB⟩:All	30.7	199	30.4	6.05	14.1	23.3	55.4	154	191
F×B−⟨FB⟩:Counts	6.58	57.1	6.05	6.05	2.02	4.67	55.4	47.3	43.1
(F×B−⟨FB⟩/F+B):All	1.3	1.0	1.3	0.99	1.3	1.3	0.90	0.99	1.1
(F×B−⟨FB⟩/F+B):Counts	1.1	0.92	0.99	0.99	1.2	1.1	0.90	0.89	0.96
FoM γ	Fiducial	xBias	No Magn	No WL	No RSD	No BAO	No WL-xBias	No RSD-xBias	No BAO-xBias
F×B:All	79	159	79	42	47	80	156	115	161
F+B:All	69	162	69	39	40	67	158	119	163
Improvement	1.1	0.99	1.1	1.1	1.2	1.2	0.98	0.97	0.99
F×B:Counts	46	156	42	42	16	47	156	109	150
F+B:Counts	39	158	39	39	11	39	158	112	149
Improvement	1.2	0.98	1.1	1.1	1.5	1.2	0.98	0.97	1.0
F:All	40	68	40	7.4	39	41	56	65	69
B:All	45	147	45	38	15	45	147	102	145
F:Counts	8.1	56	7.4	7.4	5.3	7.8	56	53	57
B:Counts	38	147	38	38	9.6	38	147	102	133
F×B−⟨$\delta_F\gamma_F$⟩:All	78	158	78	42	45	79	156	114	160
F×B−⟨$\delta_B\gamma_F$⟩:All	79	159	78	42	47	80	156	115	160
F×B−⟨$\delta\gamma$⟩:All	65	158	65	42	31	64	156	112	159
F×B−⟨FB⟩:All	76	157	76	39	46	77	153	113	158
F×B−⟨FB⟩:Counts	41	153	39	39	12	42	153	107	146
(F×B−⟨FB⟩/F+B):All	1.1	0.97	1.1	1.0	1.1	1.1	0.97	0.95	0.97
(F×B−⟨FB⟩/F+B):Counts	1.1	0.97	1.0	1.0	1.1	1.1	0.97	0.95	0.98

exact knowledge of bias would increase F×B:All and F+B:All by a factor of 6.0 and 7.9, respectively. Details on the galaxy bias are given in Paper III.

For the four defined FoMs, the survey overlap is more important when marginalizing over the bias. One example is the fiducial column, where the F×B:All/F+B:All ratio for $\mathrm{FoM}_{w\gamma}$ decreases from 1.5 to 1.1 when fixing the galaxy bias. Also, we see a lower gain from overlapping surveys when including RSD or BAO. Those effects break degeneracies between the galaxy bias and cosmology, which increase the single population cases and therefore reduce the importance of overlapping surveys. Without lensing and for a fixed bias, we find that overlapping surveys contribute negatively. This is because there are no additional counts–shear cross-correlations and

the reduced sampling variance only works with a free bias (Eriksen & Gaztañaga 2014).

If we focus on the F×B:All case, we see that the galaxy bias is the effect causing larger impact on the FoMs: fixing bias increases $\mathrm{FoM}_{w\gamma}$ by a factor of 6.0. For free bias, the most important probe is WL (factor of 4.8), then RSD (factor of 2.1) and finally BAO (factor of 1.3). If we look at FoM_γ, the order is preserved for WL (factor of 1.9) and RSD (factor of 1.7), while BAO has no impact on FoM_γ. For FoM_w or $\mathrm{FoM}_{\mathrm{DETF}}$, we see that WL is still the most important effect, but here BAO is more relevant than RSD, which makes sense as the former measures distances, while the latter measures growth, which is more relevant for FoM_γ. When bias is known (xBias), the $\mathrm{FoM}_{w\gamma}$ in overlapping surveys (F×B) and the relative

Table 5. Same as Table 4 for FoM$_w$ and FoM$_{\rm DETF}$.

FoM w	Fiducial	xBias	No Magn	No WL	No RSD	No BAO	No WL-xBias	No RSD-xBias	No BAO-xBias
F×B:All	449	1340	445	172	363	347	379	1410	1290
F+B:All	355	1190	352	159	272	267	388	1310	1120
Improvement	1.3	1.1	1.3	1.1	1.3	1.3	0.98	1.1	1.1
F×B:Counts	180	397	172	172	202	129	379	462	320
F+B:Counts	159	391	159	159	161	112	388	473	300
Improvement	1.1	1.0	1.1	1.1	1.3	1.1	0.98	0.97	1.1
F:All	77	759	77	8.7	67	67	48	804	773
B:All	174	359	174	147	179	122	310	418	297
F:Counts	9.5	51	8.7	8.7	6.8	6.4	48	55	41
B:Counts	147	310	147	147	152	100	310	373	238
F×B−⟨$\delta_F\gamma_F$⟩:All	417	1270	416	172	343	320	379	1340	1220
F×B−⟨$\delta_B\gamma_F$⟩:All	429	1310	425	172	347	330	379	1390	1260
F×B−⟨$\delta\,\gamma$⟩:All	252	635	248	172	240	186	379	705	564
F×B−⟨FB⟩:All	404	1270	400	156	309	302	361	1360	1210
F×B−⟨FB⟩:Counts	160	372	156	156	168	112	361	443	296
(F×B−⟨FB⟩/F+B):All	1.1	1.1	1.1	0.98	1.1	1.1	0.93	1.0	1.1
(F×B−⟨FB⟩/F+B):Counts	1.0	0.95	0.98	0.98	1.1	1.0	0.93	0.94	0.99
FoM DETF	**Fiducial**	**xBias**	**No Magn**	**No WL**	**No RSD**	**No BAO**	**No WL-xBias**	**No RSD-xBias**	**No BAO-xBias**
F×B:All	517	1750	512	210	535	422	981	1780	1670
F+B:All	399	1640	397	196	399	324	1050	1710	1540
Improvement	1.3	1.1	1.3	1.1	1.3	1.3	0.94	1.0	1.1
F×B:Counts	219	996	210	210	223	168	981	991	883
F+B:Counts	197	1050	196	196	208	153	1050	1050	922
Improvement	1.1	0.95	1.1	1.1	1.1	1.1	0.94	0.94	0.96
F:All	205	853	204	11	207	202	261	899	863
B:All	206	842	206	180	209	148	801	844	748
F:Counts	12	263	11	11	11	8.2	261	268	261
B:Counts	180	801	180	180	196	137	801	797	696
F×B−⟨$\delta_F\gamma_F$⟩:All	480	1700	480	210	499	389	981	1730	1620
F×B−⟨$\delta_B\gamma_F$⟩:All	495	1720	491	210	515	402	981	1750	1640
F×B−⟨$\delta\,\gamma$⟩:All	311	1140	309	210	313	236	981	1150	1030
F×B−⟨FB⟩:All	474	1670	471	191	497	382	949	1710	1580
F×B−⟨FB⟩:Counts	196	959	191	191	207	149	949	959	842
(F×B−⟨FB⟩/F+B):All	1.2	1.0	1.2	0.97	1.2	1.2	0.91	1.0	1.0
(F×B−⟨FB⟩/F+B):Counts	1.00	0.91	0.97	0.97	0.99	0.97	0.91	0.91	0.91

impact of other effects are smaller, but we have similar hierarchy of tendencies: WL (factor of 3.6), RSD (factor of 1.3) and BAO (factor of 1.04). For non-overlapping surveys (F+B) and free bias, the gain is smaller and both RSD (factor of 2.2) and BAO (factor of 1.4) become more important relative to WL (factor of 4.0).

The second section of rows is the forecast and overlapping skies ratio using only galaxy counts. The constraint without galaxy shear is lower, with F×B-All/F+B-All being 1.4, 1.2, 1.2 and 1.2 for FoM$_{w\gamma}$, FoM$_{\gamma}$, FoM$_w$ and FoM$_{\rm DETF}$. Fixing the bias of the fiducial case (xBias), the table shows how the improvement ratio becomes close to or slightly below unity, meaning all the benefit of cross-correlating the galaxy counts comes from measuring the galaxy bias. This is different from 'All' where FoM$_{w\gamma}$ and FoM$_w$, which depends both on the DE parameters and γ, improve also for a fixed bias. With shear the overlapping surveys include an additional counts–shear signal, while for counts the only benefit comes from better bias measurements. Not including RSD degrades the galaxy bias and growth determination, which is compensated for overlapping surveys which include additional cross-correlations and sample variance cancellations to better measure the galaxy bias.

The third section shows the single population constraints, with F:All and B:All, respectively, being the optimal (both counts and shear) constraints for the faint and bright population. Below are the cases F:Counts and B:Counts, which only include galaxy counts. WL is the main contribution to the faint sample, while the bright sample constraints are driven by galaxy clustering and RSD. This can be seen by comparing 'All' and 'Counts'. The ratios F:(All/Counts) and B:(All/Counts) are, respectively, 38 and 1.4 for FoM$_{w\gamma}$. In our forecast, the photometric sample uses photo-z redshifts, which drastically reduce the contribution from RSD and intrinsic galaxy counts cross-correlations between redshift bins. The low F:Counts constraints can suggest using less the current 12 faint bias parameters (71 for the bright), but the constraints would still be relatively low. Also a spectroscopic survey cannot measure shear (in B:All), but the bright includes shear when being a subset of an overlapping photometric survey.

The fourth section shows the forecast for F×B:All when not including various counts–shear cross-correlations (see notation in Table 2). The counts–shear signal is important for the combined constraints. Comparing F×B:All to F×B−⟨$\delta\,\gamma$⟩:All, we see how

FoM$_{w\gamma}$ almost doubles (2.2 times free bias) when including the counts–shear correlations, while the FoM$_w$ and FoM$_{\rm DETF}$ greatly improve (86 and 69 per cent, free bias). For FoM$_\gamma$, the change is smaller and the increase is, respectively, 22 and 1 per cent for a free and fixed bias. Including only either counts–shear cross-correlations of spectroscopic (F×B−⟨$\delta_{\rm F}\gamma_{\rm F}$⟩:All) or photometric (F×B−⟨$\delta_{\rm B}\gamma_{\rm B}$⟩:All) galaxy counts gives comparable constraints. Removing the counts–shear cross-correlations altogether (F×B−⟨$\delta\gamma$⟩:All) leads to a drastic drop. We therefore conclude that the counts–shear cross-correlations are important, but multiple populations include redundant information.

The last row section studies the direct same-sky improvement from overlapping volumes. In addition to the extra correlation, the overlapping volumes increase the covariance between different galaxy samples probing the same dark matter fluctuations. The additional covariance results in a larger covariance between the bias parameters. When marginalizing over the bias, this can improve the constraints (Eriksen & Gaztañaga 2014). The volume effect is quite small for only galaxy counts, since the constraints are mainly from the bright/spectroscopic sample. When lensing is included, the overlapping volumes measure the faint bias and therefore improve constraints through the counts–shear cross-correlations.

3.7 Magnification

In Tables 4 and 5, the 'No Magn' column removes the effect of magnification. WL increases galaxy fluxes, altering the galaxies entering into a magnitude-limited sample. Foreground matter also magnifies the area, which changes the observed galaxy densities. These two effects together are the WL magnification with number counts. Removal of magnification is done by setting the magnification slope to zero (see Fig. 1). For F×B:All, the FoM$_{w\gamma}$, FoM$_w$ and FoM$_{\rm DETF}$ improve 1 per cent from magnification, while the FoM$_\gamma$ is close to zero (<0.1 per cent). The improvement is significant when including only galaxy counts. For F×B:Counts, the magnification contributes to FoM$_{w\gamma}$, FoM$_\gamma$, FoM$_w$ and FoM$_{\rm DETF}$ with, respectively, 13, 10, 5 and 4 per cent.

In the previous paper Gaztañaga et al. (2012), we studied the impact of magnification and recently Duncan et al. (2014) confirmed those findings. One source of confusion was the notation 'MAGN', which denoted magnification combined with galaxy clustering. While stating the galaxy clustering was the main source for the constraints, the misleading labels and partly unclear text lead some readers to believe that magnification had a more central role. In this paper, the forecast of galaxy counts is simply labelled 'Counts' and includes galaxy clustering, RSD and magnification. Unlike the previous paper, this paper also discusses the effect of magnification also when including shear. We note that magnification is potentially more effective in marginalizing additional systematics (like photo-z outliers). A detailed study of constraining lensing systematics when combining with magnification is left for future work.

4 CONCLUSION

The effects of galaxy clustering, RSD, WL and BAO are presented for 2D angular cross-correlations of galaxy counts and shear. Building on Paper I, which presented the modelling, this paper uses the Fisher matrix formalism to estimate DE and growth rate (γ) constraints for photometric and spectroscopic surveys. The forecast uses two galaxy populations, one photometric (F) and one spectroscopic (B), and analyses the spectroscopic survey in 72 narrow

redshift bins to capture the radial information. All possible cross-correlations between galaxy counts and shear are included. In this paper, we focus on the relative benefit of different correlations and effects as non-linear contributions, the Limber approximation, the covariance, RSD, BAO and magnification. Details on the forecast assumptions and nomenclature can be found in Section 2.

To prevent entering into the strong non-linear regime, Section 2.2 defined a criterion for which correlations to include. In Appendix A, we study the non-linear effect, finding our $k_{\rm max}$ cut to be reasonable. In Section 3.1, we compare the benefit of different correlations. The effect of galaxy clustering, RSD and WL all enters in the 2D correlations. To investigate their relative impact, we introduce the variable $\Delta Z_{\rm Max}$, which limits the maximum distance between the mean of the two redshift bins in a correlation. For $\Delta Z_{\rm Max} = 0$, only the auto-correlations are included, then for $\Delta Z_{\rm Max} \approx 0.02$ cross-correlations between nearby bins in the spectroscopic sampling are also included, while counts–shear and magnification only enter for higher $\Delta Z_{\rm Max}$. From plotting the FoMs as a function of $\Delta Z_{\rm Max}$, we show how the different correlations contribute. This includes the cross-correlations between nearby bins in the spectroscopic sample.

The Limber approximation is widely used to simplify the calculation of the galaxy clustering in 2D correlation. As shown in Paper I, the Limber approximation only works in thick redshift bins. For narrow bins, which we need for the spectroscopic sample, the Limber approximation breaks down and incorrectly estimates zero cross-correlation for close redshift bins. Section 3.2 shows the effect on the forecast. The Limber approximation overestimates the amplitude, therefore reducing the impact of shot noise. The exact calculations give larger errors in γ than the Limber approximation. More importantly, the cross-correlations of galaxy counts in nearby bins are effective in constraining DE. Since these are zero for the Limber approximation, it leads to the exact calculation giving stronger DE constraints.

Section 3.3 studies the effect of including more bins in the spectroscopic sample. For increasing number of bins, we find that the forecast is saturating from a higher covariance. This result has previously been expected, but not shown due to technical issues with a large number of bins (Asorey et al. 2012; Di Dio et al. 2013). In the spectroscopic sample, for most bin configurations (less than 160 bins), the covariance improves the forecast. This effect comes from the covariance between redshift slices, which reduce the sample variance similar to a multi-tracer analysis (see Eriksen & Gaztañaga 2014). Lastly, we find our same-sky result to be stable over a larger number of spectroscopic bins.

In Section 3.4, we show how RSD breaks the degeneracy between the galaxy bias and f, which results in better γ constraints. Similar to the Limber subsection, the RSD/no-RSD ratio is shown as a function of $\Delta Z_{\rm Max}$. The RSD effect suppresses the galaxy counts cross-correlations of close redshift bins, which reduce their constraint. For more spectroscopic redshift bins (100 instead of 72), the RSD impact increases for the combined photometric and spectroscopic surveys. This subsection also discusses how RSD minimally impacts the signal, but decreases the counts–shear constraints through increasing galaxy counts auto-correlation which enters in the error estimate.

Opposite to RSD, the BAO contributes significantly to DE constraints, but only has a minor impact on γ constraints. Section 3.5 shows, similar to the previous subsection, the BAO/non-BAO ratio when varying $\Delta Z_{\rm Max}$ and the number of spectroscopic redshift bins. The no-BAO forecast is estimated by using the Eisenstein–Hu power spectrum without the BAO wiggles. In Paper I, we showed that the cross-correlations between narrow and close redshift bins

have a higher (radial) BAO contribution compared with the auto-correlations. This is reflected in DE constraints depending strongly on BAO when these (radial) cross-correlations are included.

Section 3.6 includes the four main forecast tabulars (Tables 4 and 5), each corresponding to a different FoM. The different rows corresponds to which galaxy populations (photometric, spectroscopic) included, if the surveys overlap observable (counts, shear) are used and if some cross-correlations are removed. Columns correspond to modifying some effect, as removing WL, magnification, RSD or BAO and if marginalizing or fixing the galaxy bias. For the combined overlapping photometric and spectroscopic survey, the bias is the physical effect with largest impact on the γ, w_0, w_a combined figure of merit FoM$_{w\gamma}$. When marginalizing over the bias (free bias), the next effective in relative importance is WL (factor of 4.8), RSD (factor 2.1), BAO (factor 1.3) and magnification (1 per cent). Magnification is discussed separately in Section 3.7, comparing with the literature and clarifying the difference in notation with Gaztañaga et al. (2012).

Two photometric (F) and spectroscopic (B) surveys increase FoM$_{w\gamma}$ equivalent to 30 per cent larger area when overlapping. The benefit is smaller for a known galaxy bias. Overlapping surveys (F×B) improve the constraints for two reasons. Additional cross-correlations for overlapping surveys can explain part of the gain. One can cross-correlate the F and B galaxy counts, and also foreground spectroscopic counts with the shear from the photometric survey. The second contribution is the additional covariance since the overlapping surveys (F and B) trace the same matter fluctuation. This advantage of two galaxy population has already been shown in 3D $P(k)$ (McDonald & Seljak 2009) and 2D correlations (Asorey et al. 2014). Here we extend those findings to WL and RSD for the combination of the F and B samples. Eriksen & Gaztañaga (2014) explain these effects in more detail and compare our forecast to other analysis in the literature.

REFERENCES

Albrecht A. et al., 2006, preprint (astro-ph/0609591)
Asorey J., Crocce M., Gaztañaga E., Lewis A., 2012, MNRAS, 427, 1891
Asorey J., Crocce M., Gaztañaga E., 2014, MNRAS, 445, 2825
Bardeen J. M., 1980, Phys. Rev. D, 22, 1882
Bernstein G. M., 2009, ApJ, 695, 652
Bernstein G. M., Cai Y.-C., 2011, MNRAS, 416, 3009
Bridle S., King L., 2007, New J. Phys., 9, 444
Cai Y.-C., Bernstein G., 2012, MNRAS, 422, 1045
Catelan P., Kamionkowski M., Blandford R. D., 2001, MNRAS, 320, L7
Chevallier M., Polarski D., 2001, Int. J. Mod. Phys. D, 10, 213
Crocce H. M., 2007, PhD thesis, New York University
de Putter R., Doré O., Takada M., 2013, preprint (arXiv:1308.6070)
Di Dio E., Montanari F., Lesgourgues J., Durrer R., 2013, preprint (arXiv:1407.0376)
Dodelson S., 2003, Modern Cosmology. Academic Press, New York
Duncan C. A. J., Joachimi B., Heavens A. F., Heymans C., Hildebrandt H., 2014, MNRAS, 437, 2471
Dvali G., Gabadadze G., Porrati M., 2000, Phys. Lett. B, 485, 208
Efstathiou G., Bernstein G., Tyson J. A., Katz N., Guhathakurta P., 1991, ApJ, 380, L47
Eisenstein D. J., Hu W., 1998, ApJ, 496, 605
Eriksen M., Gaztañaga E., 2014, preprint (arXiv:1412.8429)
Eriksen M., Gaztañaga E., 2015, MNRAS, 452, 2149 (Paper I)
Font-Ribera A., McDonald P., Mostek N., Reid B. A., Seo H.-J., Slosar A., 2013, preprint (arXiv:1308.4164)
Fry J. N., Gaztanaga E., 1993, ApJ, 413, 447
Gaztañaga E., Cabré A., Hui L., 2009, MNRAS, 399, 1663
Gaztañaga E., Eriksen M., Crocce M., Castander F. J., Fosalba P., Marti P., Miquel R., Cabré A., 2012, MNRAS, 422, 2904
Heath D. J., 1977, MNRAS, 179, 351
Heitmann K., Higdon D., White M., Habib S., Williams B. J., Lawrence E., Wagner C., 2009, ApJ, 705, 156
Heitmann K., White M., Wagner C., Habib S., Higdon D., 2010, ApJ, 715, 104
Hirata C. M., Seljak U., 2004, Phys. Rev. D, 70, 063526
Joachimi B., Bridle S. L., 2010, A&A, 523, A1
Kirk D., Lahav O., Bridle S., Jouvel S., Abdalla F. B., Frieman J. A., 2013, preprint (arXiv:1307.8062)
Lawrence E., Heitmann K., White M., Higdon D., Wagner C., Habib S., Williams B., 2010, ApJ, 713, 1322
Linder E. V., 2003, Phys. Rev. Lett., 90, 091301
Linder E. V., 2005, Phys. Rev. D, 72, 043529
McDonald P., Seljak U., 2009, J. Cosmol. Astropart. Phys., 10, 7
Martí P., Miquel R., Castander F. J., Gaztañaga E., Eriksen M., Sánchez C., 2014, MNRAS, 442, 92
Massey R. et al., 2007, ApJS, 172, 239
Matthews D. J., Newman J. A., 2010, ApJ, 721, 456
Ménard B., Scranton R., Fukugita M., Richards G., 2010, MNRAS, 405, 1025
Newman J. A., 2008, ApJ, 684, 88
Peebles P. J. E., 1980, The Large-Scale Structure of the Universe. Princeton Univ. Press, Princeton, NJ
Reid B. A. et al., 2012, MNRAS, 426, 2719
Schrabback T. et al., 2010, A&A, 516, A63
Scoccimarro R., Sheth R. K., Hui L., Jain B., 2001, ApJ, 546, 20
Scranton R. et al., 2005, ApJ, 633, 589
Seo H.-J., Eisenstein D. J., 2003, ApJ, 598, 720
Seo H.-J., Eisenstein D. J., 2007, ApJ, 665, 14
Shoji M., Jeong D., Komatsu E., 2009, ApJ, 693, 1404
Springel V., 2005, MNRAS, 364, 1105

APPENDIX A: IMPACT OF NON-LINEAR SCALES

The fiducial forecast includes Halofit-II, uses $10 \leq l \leq 300$ and removes correlations entering into non-linear scales (Section 2.2). To test the impact of non-linear scales, Fig. A1 shows the FoM$_{w\gamma}$. ratio between including non-linear $P(k)$ (Halofit II) and only the corresponding linear spectrum (from Eisenstein & Hu 1998, EH). On the x-axis is the maximum multipole included, l_{max}, which fiducially is $l_{max} = 300$. The top panel shows this ratio using all correlations until the l_{max} cut. As expected, the ratio increases with l_{max} and it is largest when including only galaxy counts.

The Halofit/Linear forecast ratio, All correlations.

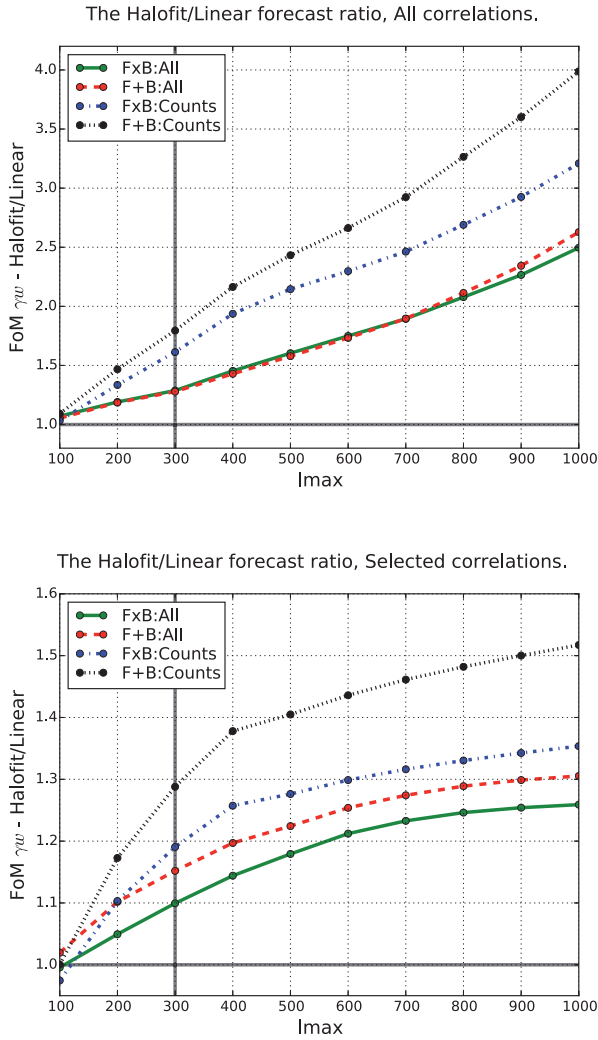The Halofit/Linear forecast ratio, Selected correlations.

Figure A1. Forecast ratio between including the Halofit contributions and only the linear (Eisenstein & Hu 1998, EH) power spectrum. The figure of merit is FoM$_{w\gamma}$ and the lines correspond to F×B:All, F+B:All, F×B:Counts and F+B:Counts. In the top/bottom panel, the ratios include/exclude correlations entering into non-linear scales ($k > k_{max}$). A vertical line at $l_{max} = 300$ marks the fiducial value.

Tri-contour plot, Galaxy Shear and Counts.

Tri contour plot, Galaxy Counts.

Figure B1. Contour plots of w_0, w_a and γ. The three sub-plots show the Fisher matrix 1σ contours, marginalizing over the DETF parameters and galaxy bias. The top panel shows contours for F×B:All, F+B:All, B:All and F:All, while the bottom panel only includes galaxy counts.

The bottom panel illustrates the effect of an additional cut to remove correlations entering into non-linear scales $k > k_{max}$. For $l_{max} = 300$, the FoM$_{w\gamma}$ including Halofit is for F×B:Counts, respectively, 30 and 80 per cent higher than EH only when removing or using all correlations. With the increase in l_{max}, the ratio with 'All' correlations grows quite linearly, while for the 'selected correlations' the ratio flattens. The FoM$_{\rm DETF}$ and FoM$_\gamma$ (not shown) follow the same pattern, but with smaller ratios. For FoM$_w$ (not shown), the ratios are even flatter at high l_{max} and none of the probes cross the line 1.2. The fiducial forecast includes Halofit, but we limit the correlations included to not become too sensitive to assumptions on the non-linear scales. In addition to the non-linear matter power spectrum, these scales could require a scale-dependent galaxy bias. Note that these results are on the forecast accuracy, which mainly depends on the observable derivative with respect to cosmology. The cut in non-linear scales for not biasing a parameter fit (precision) can be different and is not considered here.
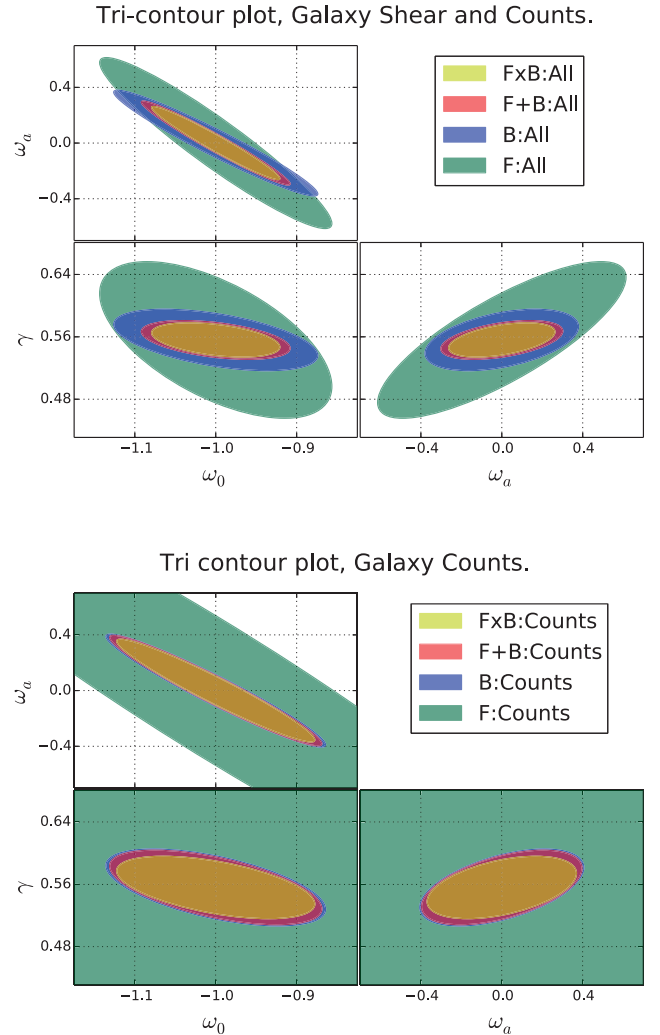
APPENDIX B: CONTOURS

Fig. B1 shows the 1σ contours for w_0, w_a and γ. The top panel shows for 'All' and the combination F×B, F+B, F and B. One can see that some trends are also present in the tables. The combination F+B:All, combining shear and galaxy counts from separate surveys, is more powerful than analysing the survey separately. The factor of 1.5 improvement of F×B:All over F+B:All corresponds to the difference between the two inner ellipses. On the bottom is a similar plot for the galaxy counts. Using equal scales allows us to directly compare the constraints, but at the expense of the F:Counts contours being plotted beyond the borders. For the galaxy counts, the bright population completely dominates, even if the bright sample includes more bias parameters.

Fig. B2 looks at the effect of removing WL and RSD. The equivalent magnification and BAO plots are not included since those effects are weaker, which results in less difference between the ellipses. The top panel shows F×B:All and F+B:All in a tricontour plot, with and without WL (fiducial and 'No Lens'). The WL

Tri-contour plot, Removing Lensing.

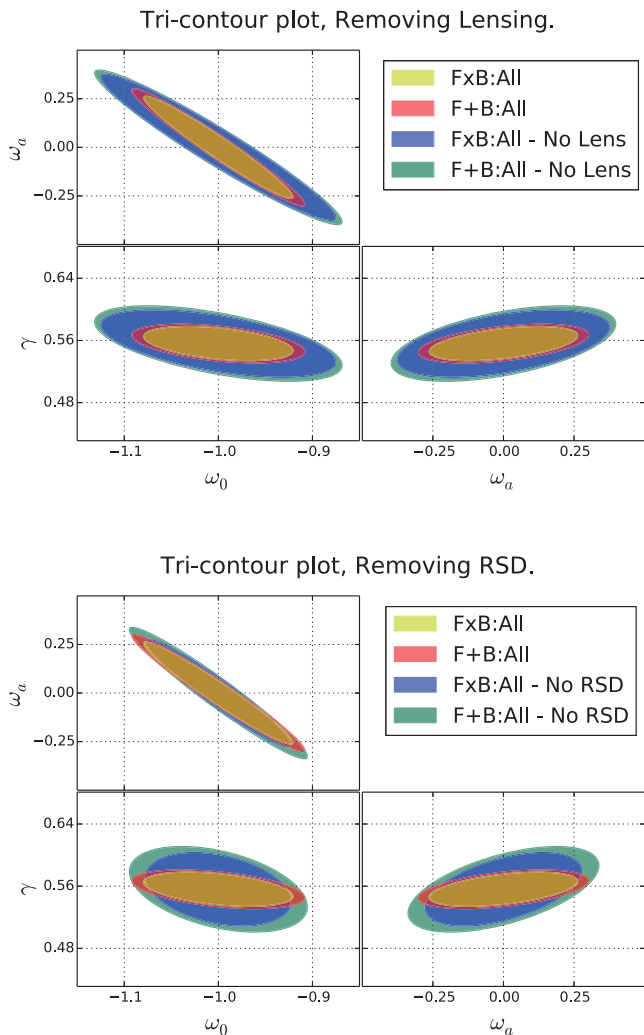## Tri-contour plot, Removing RSD.

Figure B2. Contour plots of w_0, w_a and γ. The three sub-plots show the Fisher matrix 1σ contours, marginalizing over the DETF parameters and galaxy bias. In the upper plot, two ellipses are the fiducial F×B:All and F+B:All, while two remove WL observables. The bottom plot similarly shows the fiducial F×B:All and F+B:All, and then two contours in real space.

improves the constraints on all three parameters included in the contour plots. Comparing the FoMs in Tables 4 and 5, one can see that same-sky benefit of F×B:All is actually higher when including lensing.

In the lower panel is a similar plot, instead with two contours calculated with and without RSD (fiducial and 'No RSD'). While the RSD impact the parameter constraints different, the margins are exactly equal so one can visually compare the effects. The RSD is contributing strongly to measuring γ and less to w_0 and w_a. One can also see the same trend in Tables 4 and 5. There the RSD improves $\mathrm{FoM}_{w\gamma}$, FoM_γ and FoM_w which depends on γ, while not $\mathrm{FoM}_{\mathrm{DETF}}$ where γ is fixed. The difference between the contours in bottom panel shows that RSD increases or decreases the importance of overlapping surveys. Including RSD, looking at the numerical values in the table, slightly reduces the benefit of overlapping galaxy surveys.

This paper has been typeset from a TEX/LATEX file prepared by the author.